Measurement of the Branching Fraction for $K_L^0 \to \mu^+\mu^-e^+e^-$

Andrew J. Norman

January 2004

BNL E871 Collaboration

D. Ambrose, S. Graessle, G. W. Hoffmann, J. McDonough, A. Milder, P.J. Riley, J.L. Ritchie, V.I. Vassilakopoulos, C.B. Ware, S. Worm

University of Texas, Austin, Texas 78712

C. Arroyo, K.M. Ecklund, K. Hartman, M. Hebert, G.M. Irwin, M. Pommot-Maia, S.G. Wojcicki

Stanford University, Stanford, California 94305

M. Bachman, P. de Cecco, D. Connor, N. Kanematsu, R. Lee, W.R. Molzon

University of California, Irvine, California 92697

M. Eckhause, A.D. Hancock, C.H. Hoff, J.R. Kane, Y. Kuang, R.D. Martin, R.E. Welsh, E. Wolin

College of William and Mary, Williamsburg, Virginia 23187

P.D. Rubin

University of Richmond, Richmond, Virginia 94305

Collaboration Publications

Improved branching ratio measurement of the decay $K_L^0 \to \mu^+\mu^-$. [1]

First observation of the rare decay mode $K_L^0 \to e^+e^-$. [2]

New limit on muon and electron lepton number violation from $K_L^0 \to \mu^\pm e^\mp$ decay. [3]

A compact beam stop for a rare kaon decay experiment. [4]

Introduction

W&M HEG worked on extracting $B(K_L^0 \to \mu^+\mu^-e^+e^-)$ from E871.

Measurement was made along side measurements of $B(K_L^0 \to \mu^+\mu^-)$ and $B(K_L^0 \to e^+e^-)$ in order to extract information on the $K_L^0 \to \gamma^*\gamma^*$ vertex with similar systematics to the dileptonic decays.

The combination of $B(K_L^0 \to \mu^+\mu^-e^+e^-)$, $B(K_L^0 \to \mu^+\mu^-)$ and the unitary bound give information on the CKM elements relating *top* and *charm* quarks.

$K_L^0 \to \mu^+\mu^-e^+e^-$ decay spectrum is dependent on the type of form factor used to compute the decay. In principle it is possible to distinguish between a VDM, χPT, or CP violating form factor.

Introduction (cont.)

Prior to the start of this analysis there was one event reported with a branching fraction of $2.9^{+6.7}_{-2.4} \times 10^{-9}$ by the KTeV experiment E799 [5].

- This result spanned almost a full order of magnitude in it's uncertainty.
- No differentiation between form factor models.
- Extraction of $K_{\gamma^*\gamma^*}$ vertex and $\mathscr{A}_{LD}$ suffer large uncertainties.

During the analysis, 43 additional events were reported by the KTeV collaboration[6], with branching ratio of 2.62×10^{-9}.

- Still not enough data to differentiate between models.

Part I

Theory and Background

Standard Model

Leptons are grouped into *flavor* doublets:

$$\begin{pmatrix} e \\ \nu_e \end{pmatrix} \qquad \begin{pmatrix} \mu \\ \nu_\mu \end{pmatrix} \qquad \begin{pmatrix} \tau \\ \nu_\tau \end{pmatrix} \tag{1}$$

Defines the "lepton number" L_ℓ
Processes that do not conserve L_ℓ are "Lepton Flavor Violating".

Mixing between e, μ and τ has not been observed, but there are projects under way to look for it [7, 8]
Evidence for mixing between ν_e, ν_μ and ν_τ exists from various sources.

Standard Model (cont.)

Similarly the quarks form doublets:

$$\begin{pmatrix} u \\ d \end{pmatrix} \qquad \begin{pmatrix} c \\ s \end{pmatrix} \qquad \begin{pmatrix} t \\ b \end{pmatrix} \tag{2}$$

Defines the quantum numbers for Isospin (I_z), Strangeness (S), Charm, Top and Bottom.

Horizontal mixing of quark flavors is observed through Cabibbo mixing:

$$\begin{pmatrix} u \\ d' \end{pmatrix}_L = \begin{pmatrix} u \\ d\cos\theta_C + s\sin\theta_c \end{pmatrix}_L \tag{3}$$

Cabbibo Mixing

Mixing leads to weak charged and neutral currents:

$$J_\mu^{CC} = (\bar{d}\cos\theta_C + \bar{s}\sin\theta_C)\gamma_\mu(1-\gamma_5)u\ , \quad \text{and} \tag{4}$$

$$J_\mu^{NC} = (\bar{d}\cos\theta_C + \bar{s}\sin\theta_C)\gamma_\mu(1-\gamma_5)(d\cos\theta_C + s\sin\theta_C) \tag{5}$$

- Taking G as the weak coupling, the charged current $\Delta S = 0$ couple as $G\cos\theta_C$, while the $\Delta S = 1$ interactions are suppressed by $G\sin\theta_C$ or approximately $\sin^2\theta_C \sim \frac{1}{20}$.

For the neutral current the process becomes:

$$u\bar{u} + d'\bar{d}' = \underbrace{u\bar{u} + (d\bar{d}\cos^2\theta_C + s\bar{s}\sin^2\theta_C}_{\Delta S=0} + \underbrace{(s\bar{d} + d\bar{s})\cos\theta_C\sin\theta_C}_{\Delta S=1} \tag{6}$$

- The $\Delta S = 1$, first order flavor changing neutral current is now suppressed by $\cos\theta_C \sin\theta_C$.

Still not enough suppression to account for $B(K_L^0 \to \mu^+\mu^-)$!

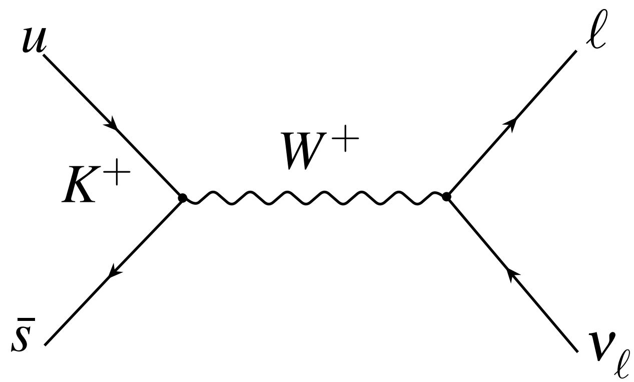

(a) Weak flavor changing charged current diagram for $K^+ \to \ell^+ \nu$

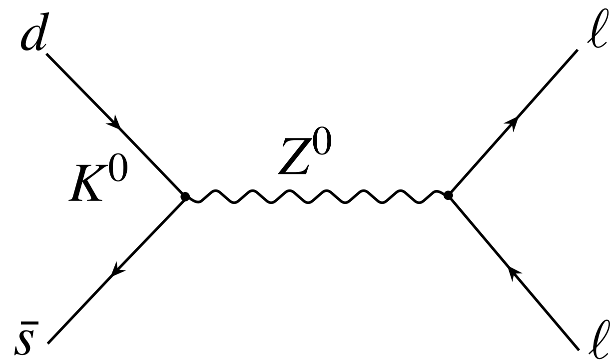

(b) Weak flavor changing neutral current diagram for $K^0 \to \ell\ell$

FIG. 1: First order weak flavor changing kaon decay processes

GIM Mechanism

How do we explain the observed suppression of $K_L^0 \to \mu^+\mu^-$?

Glashow, Iliopoulus and Maiani (GIM) proposed a second mixing doublet with a *charm* quark.

$$\begin{pmatrix} c \\ s' \end{pmatrix} = \begin{pmatrix} c \\ s\cos\theta_C - d\sin\theta_C \end{pmatrix} \tag{7}$$

The neutral current now becomes:

$$u\bar{u} + d'\bar{d}' + c\bar{c} + s'\bar{s}' = \underbrace{u\bar{u} + c\bar{c} + (d\bar{d} + s\bar{s})\cos^2\theta_C + (d\bar{d} + s\bar{s})\sin^2\theta_C}_{\Delta S=0}$$
$$+ \underbrace{(s\bar{d} + \bar{s}d - \bar{s}d - s\bar{d})\sin\theta_C\cos\theta_C}_{\Delta S=1} \tag{8}$$

The $\Delta S = 1$ contribution cancels EXACTLY at first order!

GIM (cont.)

More generally the quark mixing can be expressed via a *Mixing Matrix* V_{ij}. So for *down* type quarks (d,s,b) mixing is expressed as:

$$q'_i = \sum_j V_{ij} q_j \tag{9}$$

The GIM identity then states:

$$\begin{aligned} \sum_i^N \bar{q}'_i q'_i &= \sum_i^N \sum_j^N \sum_k^N \bar{q}_i V_{ij}^{\dagger} V_{jk} q_k \\ &= \sum_i^N \bar{q}_i q_i \end{aligned} \tag{10}$$

There are no first order Flavor Changing Neutral Currents (FCNC).

Additionally second order FCNC diagram approximately cancel leading to addition suppression proportional to $\cos\theta_C \sin\theta_C$

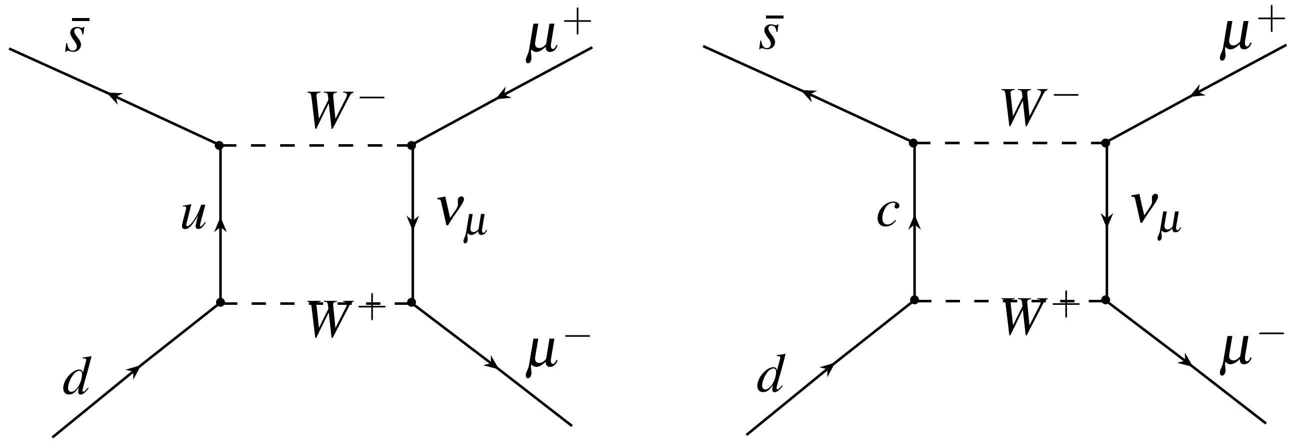

(a) Up quark contribution to $K_L^0 \to \mu^+\mu^-$

(b) Charm quark contribution to $K_L^0 \to \mu^+\mu^-$

FIG. 2: Second order weak $\Delta S = 1$ contributions to $\Gamma(K_L^0 \to \mu^+\mu^-)$ which approximately cancel through the GIM mechanism

CKM Matrix

Generalization of the Cabibbo mixing leads to the generalized rotation matrix of Kobayashi and Maskawa [9].

The 3×3 CKM matrix mixes the *down-like* charge $-\frac{1}{3}$ quarks.

$$\begin{pmatrix} d' \\ s' \\ b' \end{pmatrix} = \begin{pmatrix} V_{ud} & V_{us} & V_{ub} \\ V_{cd} & V_{cs} & V_{cb} \\ V_{td} & V_{ts} & V_{tb} \end{pmatrix} \begin{pmatrix} d \\ s \\ b \end{pmatrix} \tag{11}$$

The matrix is unitary resulting in three independent real parameters, the mixing angles $(\theta_1, \theta_2, \theta_3)$ and one phase δ.

It can be expressed as:

$$V_{CKM} = \begin{pmatrix} c_1 & -s_1 c_3 & -s_1 s_3 \\ s_1 c_2 & c_1 c_2 c_3 - s_2 s_3 e^{i\delta} & c_1 c_2 s_3 + s_2 c_3 e^{i\delta} \\ s_1 s_2 & c_1 s_2 c_3 + c_2 s_3 e^{i\delta} & c_1 s_2 s_3 - c_2 c_3 e^{i\delta} \end{pmatrix} \tag{12}$$

where:

$$c_i \equiv \cos\theta_i \quad \text{and} \quad s_i \equiv \sin\theta_i. \tag{13}$$

A non-zero value of the phase δ leads to off diagonal contributions to to V_{cb} and V_{ts}.

These off diagonal terms break the CP invariance of the weak interaction.

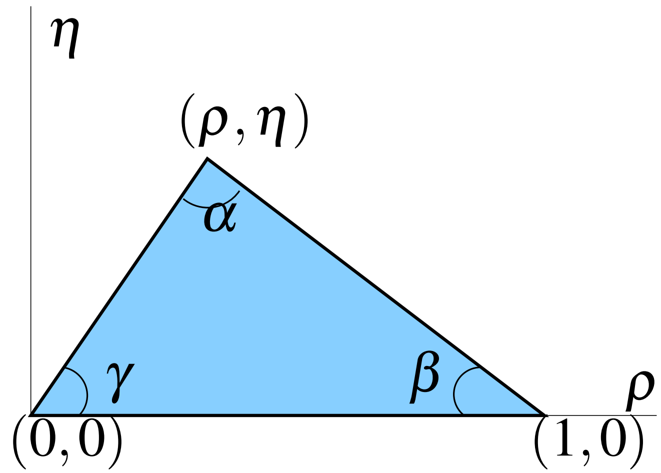

FIG. 3: Geometric representation of the unitary triangle

The CKM matrix can be related to the unitary triangle by expanding in powers of the Cabibbo angle $\lambda = |V_{us}|$.

$$\mathbf{V} = \begin{pmatrix} 1-\frac{1}{2}\lambda^2 & \lambda & A\lambda^3(\rho - \imath\eta) \\ -\lambda & 1-\frac{1}{2}\lambda^2 & A\lambda^2 \\ A\lambda^3(1-\rho-\imath\eta) & -A\lambda^2 & 1 \end{pmatrix} \tag{14}$$

Wolfenstein Parameterization

This is the Wolfenstein parameterization of the CKM matrix.

The CKM matrix in this form can further be expanded to require unitarity. Imposing unitarity on the imaginary part to $\mathscr{O}(\lambda^5)$ and the real part to $\mathscr{O}(\lambda^3)$, the Wolfenstein representation becomes:

$$\mathbf{V} = \begin{pmatrix} 1-\frac{1}{2}\lambda^2 & \lambda & A\lambda^3(\rho - \imath\eta + \frac{1}{2}\imath\eta\lambda^2) \\ -\lambda & 1-\frac{1}{2}\lambda^2 - \imath\eta A^2\lambda^4 & A\lambda^2(1+\imath\eta\lambda^2) \\ A\lambda^3(1-\rho-\imath\eta) & -A\lambda^2 & 1 \end{pmatrix} \tag{15}$$

- All the CP violating terms are now $\mathscr{O}(\lambda^3)$.
- We can directly relate these CP terms to $K^{\pm}$ and K^0 decays!

Unitary Bound

We can divide the decay rate into real and imaginary parts

$$B(K_L^0 \to \ell^+\ell^-) = |Re\mathscr{A}|^2 + |Im\mathscr{A}|^2 \tag{16}$$

In analogy to a scattering amplitude, the real component is the *dispersive* amplitude and the imaginary component is the *absorptive* amplitude.

Since $K_L^0 \to \ell^+\ell^-$ has contributions from both the Weak interaction and the electro-magnetic interactions, the amplitude is divided as:

$$\mathscr{A} = (\mathscr{A}_{disp,weak} + \mathscr{A}_{disp,ld}) + \imath(\mathscr{A}_{abs,weak} + \mathscr{A}_{abs,ld}) \tag{17}$$

Unitary Bound (cont.)

The weak absorptive amplitude, $\mathscr{A}_{abs,weak}$ is explicitly zero.

The branching fraction can be written in the traditional notation as:

$$\begin{aligned} B(K_L^0 \to \ell^+\ell^-) &= |\mathscr{A}_{disp}|^2 + |\mathscr{A}_{abs}|^2 \\ &= |\mathscr{A}_{weak} + \mathscr{A}_{ld}|^2 + |\mathscr{A}_{abs}|^2 \end{aligned} \tag{18}$$

The absorptive portion of the amplitude is dominated by a real two photon intermediate state as shown in Fig. 4.

- This diagram can be calculated from QED.
- This is the *"unitary diagram."*

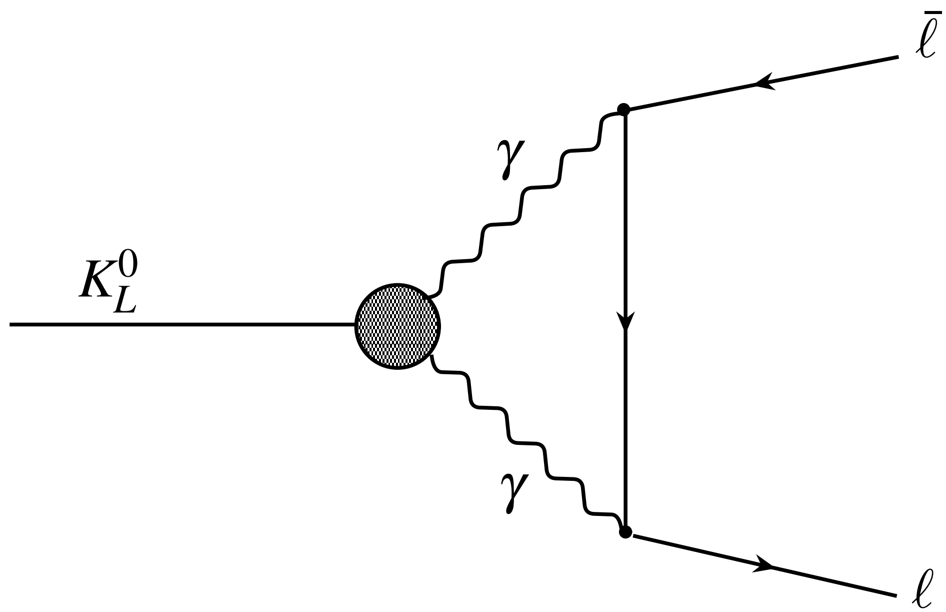

FIG. 4: Leading order absorptive contribution to $K_L^0 \to \ell\bar{\ell}$ via a real two photon intermediate state

Unitary Limits

Decay Branch	Unitary Bound	Observation
$B(K_L^0 \to \gamma\gamma)$	N/A	$(5.96 \pm 0.15) \times 10^{-4}$
$B(K_L^0 \to e^+e^-)/B(K_L^0 \to \gamma\gamma)$	1.19×10^{-5}	N/A
$B(K_L^0 \to \mu^+\mu^-)/B(K_L^0 \to \gamma\gamma)$	5.32×10^{-9}	N/A
$B(K_L^0 \to e^+e^-)$	$(3.15 \pm 0.08) \times 10^{-12}$	$\left(9^{+6}_{-4}\right) \times 10^{-12}$
$B(K_L^0 \to \mu^+\mu^-)$	$(7.04 \pm 0.18) \times 10^{-9}$	$(7.25 \pm 0.16) \times 10^{-9}$

TABLE 1: Unitary limits on dilepton decays of K_L^0

The $K_L^0 \to \mu^+\mu^-$ branching fraction abuts the unitary bound.

The K Meson

The neutral K meson was first reported to have been observed in 1947 by G. Rochester and C. Butler[10].

It is observed to have a mass roughly 900 times that of the electron.

The neutral Kaon is a two quark bound state containing a *strange* quark.

$$K^0 = |\bar{s}d\rangle \quad \text{and} \quad \bar{K}^0 = \left|s\bar{d}\right\rangle \tag{19}$$

The quantum numbers for the Kaon include the "strangeness" S.

$$S\left|K^0\right\rangle = +\left|K^0\right\rangle \qquad S\left|\bar{K}^0\right\rangle = -\left|\bar{K}^0\right\rangle \tag{20}$$

Kaon Quantum Numbers

$$
\begin{aligned}
Spin &= 0 \\
Parity &= -1 \ \ \text{(pseudoscalar)} \\
K^0 : T = \frac{1}{2}\ ,\ T_3 &= -\frac{1}{2}\ ,\ S = +1 \\
\bar{K}^0 : T = \frac{1}{2}\ ,\ T_3 &= +\frac{1}{2}\ ,\ S = -1
\end{aligned}
\tag{21}
$$

Kaon Mixing

Due to the presence of the strangeness changing weak interaction, the kaon exhibits strangeness oscillations and regeneration effect unique to the K system.

Oscillations occur through $\Delta S = 2$ interactions (pion loops).

$$\left|K^0(t)\right\rangle \rightarrow a(t)\left|K^0\right\rangle + b(t)\left|\bar{K}^0\right\rangle \tag{22}$$

Weak splitting of the Hamiltonian leads us to write the kaon states as linear combinations of new observables $\left|K_1^0\right\rangle$ and $\left|K_2^0\right\rangle$.

$$\left|K^0\right\rangle = \left(a\left|K_1^0\right\rangle + b\left|K_2^0\right\rangle\right)/\sqrt{a^2+b^2} \tag{23}$$

$$\left|\bar{K}^0\right\rangle = \left(c\left|K_1^0\right\rangle + d\left|K_2^0\right\rangle\right)/\sqrt{c^2+d^2} \tag{24}$$

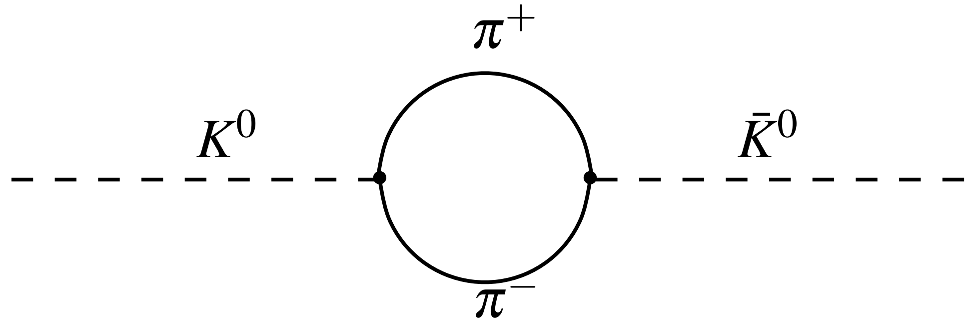

FIG. 5: K^0 to $\bar{K}^0$ mixing via an intermediate pion loop

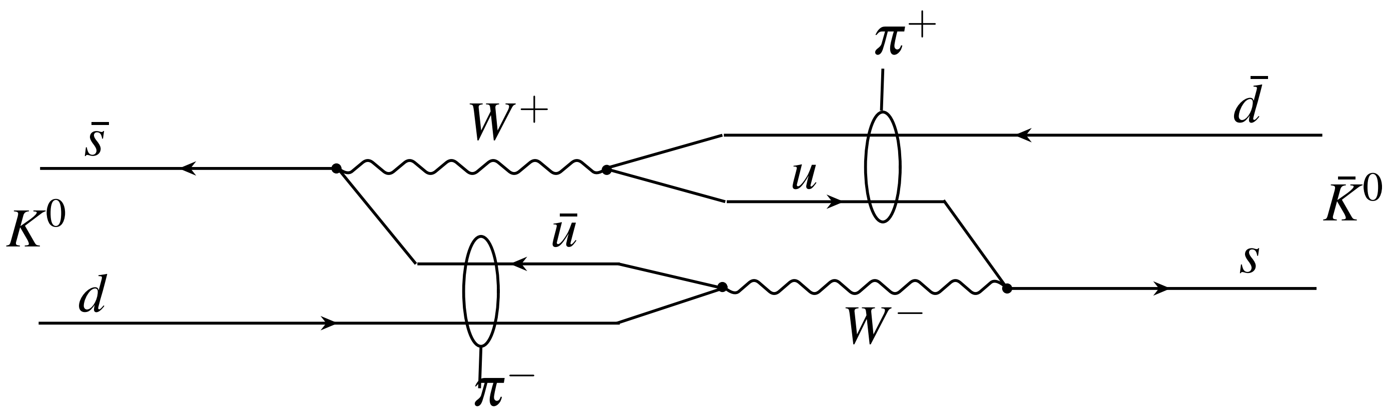

FIG. 6: K^0 to $\bar{K}^0$ mixing via a second order $\Delta S = 2$ weak interaction

CP Symmetries

The strange eigenstates K^0 and $\bar{K}^0$ transform into one another under $\hat{C}\hat{P}$.

$$\hat{C}\hat{P}\left|K^0\right\rangle = -\left|\bar{K}^0\right\rangle \qquad \hat{C}\hat{P}\left|\bar{K}^0\right\rangle = -\left|K^0\right\rangle \tag{25}$$

K^0 and $\bar{K}^0$ are clearly NOT the CP eigenstates. Instead use a linear combination:

$$\begin{aligned} \left|K_1^0\right\rangle &\equiv \frac{1}{\sqrt{2}}\left[\left|K^0\right\rangle + \left|\bar{K}^0\right\rangle\right] \\ \left|K_2^0\right\rangle &\equiv \frac{1}{\sqrt{2}}\left[\left|K^0\right\rangle - \left|\bar{K}^0\right\rangle\right] \end{aligned} \tag{26}$$

The weak eigenstates are now states of definite $\hat{C}\hat{P}$:

$$\begin{aligned} \hat{C}\hat{P}\left|K_1^0\right\rangle &= +\left|K_1^0\right\rangle \\ \hat{C}\hat{P}\left|K_2^0\right\rangle &= -\left|K_2^0\right\rangle \end{aligned} \tag{27}$$

K_L^0 and K_S^0

Kaons can be produced through a strong interaction using associated hyperon production:

$$\pi^- p \rightarrow K^0 \Lambda \tag{28}$$

Experimentally we do observe two distinct neutral kaons with radically different lifetimes. We denote these as the Short-lived (K_S^0) and Long-lived Kaons (K_L^0).

Kaon Species	Lifetime τ (s)	$c\tau$	Spin	$\hat{C}\hat{P}$
K_S^0	0.89×10^{-10}	2.67 cm	0	even
K_L^0	5.17×10^{-8}	15.51 m	0	odd

TABLE 2: Experimentally observed kaon properties

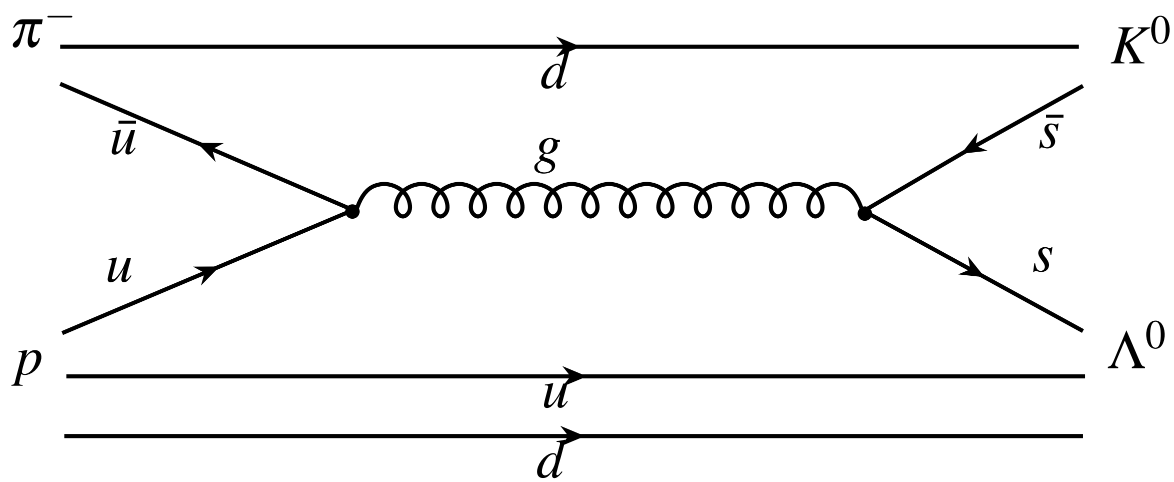

FIG. 7: Strong interaction production of a neutral kaon through associated Λ^0 hyperon production.

- A beam of kaons initially contains an equal proportion of K_S^0 and K_L^0.
- To obtain a pure K_L^0 beam, force the short-lived component decay out.

CP Violation

In 1964 Fitch and Cronin[11] observed the decay of K_L^0 into a two pion final state. This demonstrated that the $\hat{C}\hat{P}$ symmetry of the standard model is not exact.

In fact B($K_L^0 \rightarrow \pi^+\pi^-$) $= 0.2067 \pm 0.035\%$ [12], meaning roughly 1 in 500 decays of K_L^0 violate $\hat{C}\hat{P}$!

While strongly suppressed, the $\hat{C}\hat{P}$ symmetry is violated in weak decays.

This means that for CPT to hold, time reversal invariance must also be violated!

As a result the transition amplitudes for $K^0 \leftrightarrow \bar{K}^0$ oscillations are not equal:

$$\left\langle K^0 \right| \hat{\mathscr{S}} \left| \bar{K}^0 \right\rangle \neq \left\langle \bar{K}^0 \right| \hat{\mathscr{S}} \left| K^0 \right\rangle \tag{29}$$

To quantify this CP violation we rewrite the weak eigenstates K_S^0 and K_L^0 in terms of the true CP eigenstates K_1^0 and K_2^0 and allow for a slight mixing of the states through a violation parameter ε:

$$\begin{aligned} \left|K_S^0\right\rangle &= \frac{1}{\sqrt{1+|\varepsilon|^2}}\left(\left|K_1^0\right\rangle + \varepsilon\left|K_2^0\right\rangle\right) \\ \left|K_L^0\right\rangle &= \frac{1}{\sqrt{1+|\varepsilon|^2}}\left(\left|K_2^0\right\rangle + \varepsilon\left|K_1^0\right\rangle\right) \end{aligned} \tag{30}$$

Experimentally the parameter $\varepsilon \approx 2.3 \times 10^{-3}$.

CP Violation (Aside)

The semi-leptonic decay modes:

$$
\begin{aligned}
K_L^0 \rightarrow \pi^- \mu^+ \nu_\mu \quad &\text{and} \quad K_L^0 \rightarrow \pi^+ \mu^- \nu_\mu \\
K_L^0 \rightarrow \pi^- e^+ \nu_e \quad &\text{and} \quad K_L^0 \rightarrow \pi^+ e^- \nu_e
\end{aligned}
\tag{31}
$$

Exhibit a very slight asymmetry between their charge conjugate decay modes.

The asymmetry allows us to find the $\hat{C}\hat{P}$ violating phase δ from the CKM matrix.

$$
\delta = \frac{\Gamma\left(K_L^0 \rightarrow \pi^- \ell^+ \nu_\ell\right) - \Gamma\left(K_L^0 \rightarrow \pi^+ \ell^- \nu_\ell\right)}{\Gamma\left(K_L^0 \rightarrow \pi^- \ell^+ \nu_\ell\right) + \Gamma\left(K_L^0 \rightarrow \pi^+ \ell^- \nu_\ell\right)}
\tag{32}
$$

Matter/Anti-Matter Asymmetry

- The semi-leptonic asymmetry is $0.327 \pm 0.012\%$
- The semi-leptonic asymmetry is a matter/anti-matter asymmetry
- The semi-leptonic asymmetry provide the unique distinction between particles and anti-particles
- The semi-leptonic asymmetry proves the absolute definition of positive electric charge, as being that flavor of lepton which is preferred in the decay of the neutral kaon!

Part II

$K_L^0 \to \gamma^* \gamma^*$ and $K_L^0 \to \mu^+ \mu^- e^+ e^-$

$\mathscr{A}_{LD}$ and $K_L^0 \to \gamma^*\gamma^*$

The dispersive contribution to $K_L^0 \to \ell^+\ell^-$ can be divided into the weak and the long distance electromagnetic amplitudes.

$$Re\mathscr{A} = \mathscr{A}_{SD} + \mathscr{A}_{LD} \tag{33}$$

GIM cancellation of the tree level FCNC leave A_{SD} confined to the second order box and penguin diagrams.

To determine the contribution of these diagrams B($K_L^0 \to \mu^+\mu^-$) can be related to the charged current process $K^+ \to \pi^+\nu\bar{\nu}$[13].

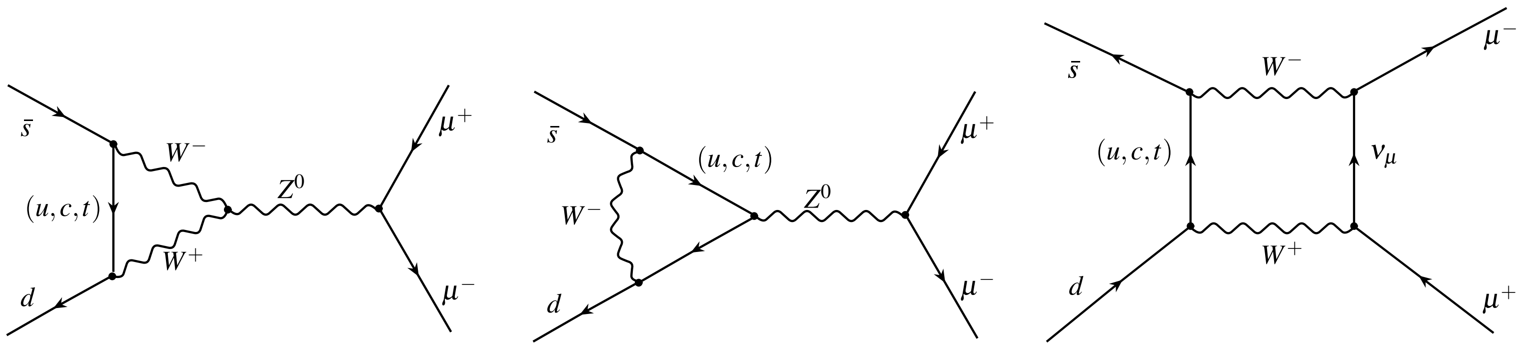

(a) Weak Penguin Diagram

(b) Weak Penguin Diagram

(c) Weak Box Diagram

FIG. 8: Short distance weak diagrams contributing to $K_L^0 \to \mu^+\mu^-$

The amplitude can be written as*:

$$Re(\mathscr{A})_{SD} = \frac{\alpha^2}{4\pi^2 \sin^4\theta_W} \frac{(1-4m_\mu^2/M_K^2)^{1/2}}{(1-m_\mu^2/M_K^2)^2} \frac{\left| Re \sum_{i=c,t} \eta_i V_{is}^* V_{id} C_\mu(x_i) \right|^2}{|V_{us}|^2} \tag{34}$$

The *top* quark diagrams dominate the short distance contribution. As a result we relate the CKM matrix elements to the Wolfenstein parameterization:

$$Re(V_{ts}^* V_{td}) = -A^2\lambda^5(1-\rho) \tag{35}$$

$$Re(V_{cs}^* V_{cd}) = -(\lambda - \frac{1}{2}\lambda^2) \tag{36}$$

---

* η_i are the QCD corrections, $C(x_{up}) \approx 10^{-9}$, $C(x_{charm}) \approx 3 \times 10^{-3}$, $C(x_{top}) \approx 2.1$

As a result the short distance $K_L^0 \to \mu^+\mu^-$ amplitude becomes:

$$|\mathscr{A}_{SD}|^2 = (4.17 \times 10^{-10}) A^4 \, |\eta_t C(x_t)|^2 \left[1 - \rho + \frac{474 \eta_c C(x_c)}{A^2 \eta_t C(x_t)} \right]^2 \tag{37}$$

The top quark dominates, which means simply:

$$|\mathscr{A}_{SD}|^2 \propto (1 - \rho)^2 \tag{38}$$

- Measuring B($K_L^0 \to \mu^+\mu^-$) gives the Wolfenstein ρ!

$K_{\gamma^*\gamma^*}$ Vertex

To extract the Wolfenstein ρ from $B(K_L^0 \to \mu^+\mu^-)$ we need knowledge of $\mathscr{A}_{LD}$.

$\mathscr{A}_{LD}$ is found from the class of diagrams shown in Fig. 9 involving the exchange of two virtual photons.

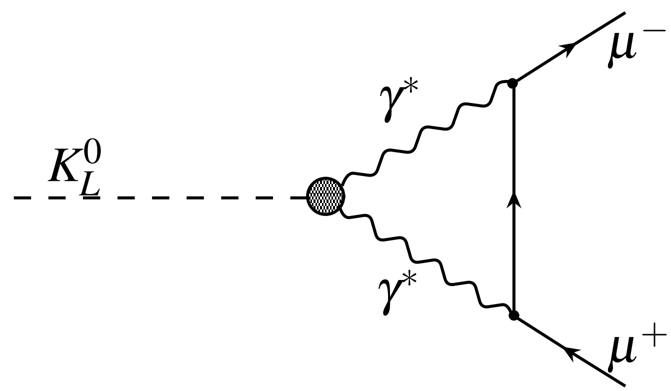

FIG. 9: Long distance dispersive diagram for $K_L^0 \to \mu^+\mu^-$ involving the exchange of two virtual photons.

$K_{\gamma^*\gamma^*}$ Model Dependence

Calculation of the $K_{\gamma^*\gamma^*}$ vertex requires knowledge of a form factor, $F(q_1^2, q_2^2)$.

The manner in which of the form factor is computed is model dependent.

The theories that we examined for calculating $F(q_1^2, q_2^2)$ were:

- **VDM** - need $K_L^0 \to \ell\bar{\ell}\gamma$ and $K_L^0 \to \ell\bar{\ell}\ell'\bar{\ell}'$ information
- **QCD** - low energy perturbative, need $K_L^0 \to \ell\bar{\ell}\gamma$ and $K_L^0 \to \ell\bar{\ell}\ell'\bar{\ell}'$ information for parameter fits
- χ**PT** - low energy, provides enhancement in high invariant mass region, works for $K_L^0 \to \mu^+\mu^-\gamma$
- **CP Violating** - allows for access to CP violation through knowledge of the angular distribution ϕ and B($K_L^0 \to \mu^+\mu^-e^+e^-$)

VDM Diagrams

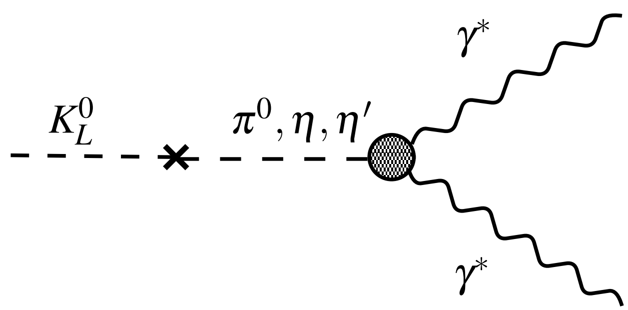

(a) $\Delta S = 1$ transition on meson leg

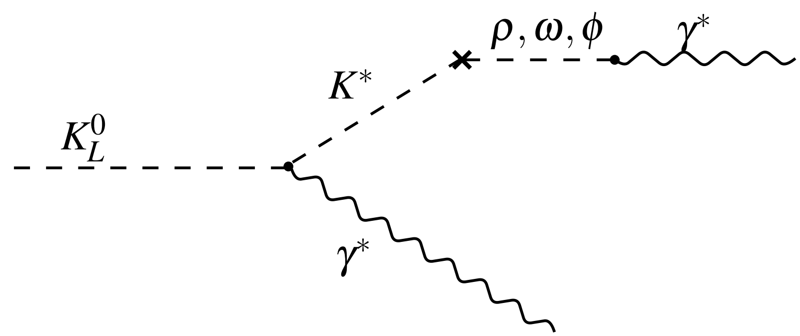

(b) $\Delta S = 1$ transition on photon leg

FIG. 10: Long distance dispersive pole diagram for $K_L^0 \to \gamma^* \gamma^*$ as proposed by Bergstrom, Masso, Singer, et. al. [14]

More VDM Diagrams

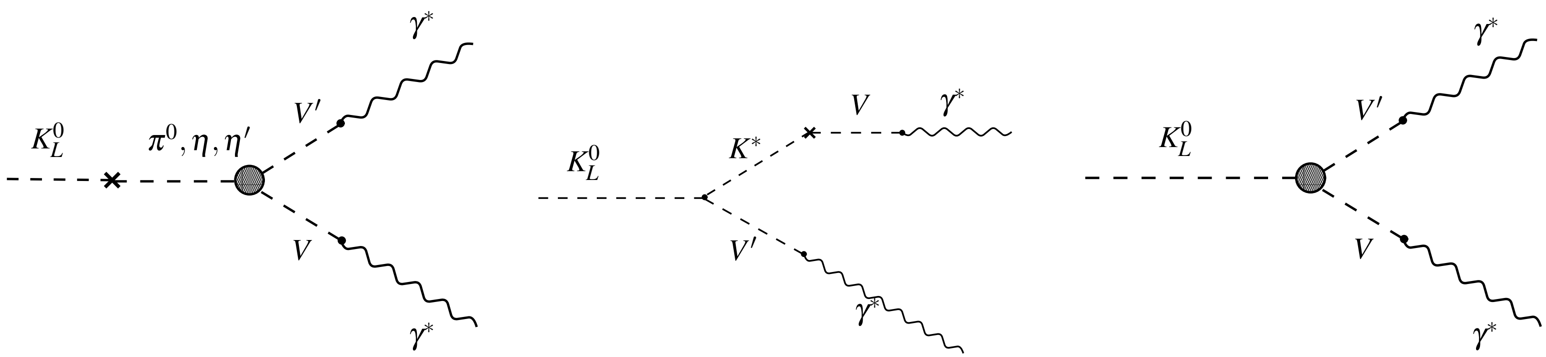

(a) A (b) B (c) C

FIG. 11: Long distance dispersive diagram for $K_L^0 \to \gamma^*\gamma^*$ as proposed by Ko involving vector meson couplings. [15]

QCD Diagrams

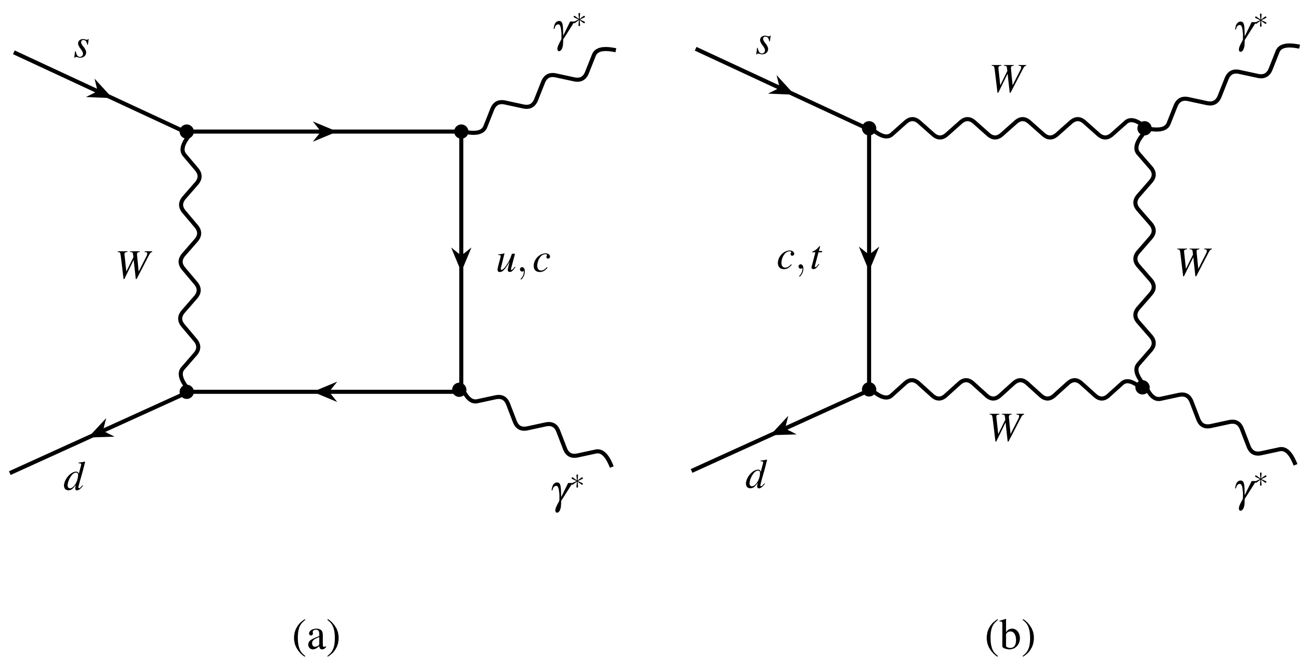

FIG. 12: Loop order QCD diagrams contributing to $K_L^0 \to \gamma^* \gamma^*$. [16]

More QCD Diagrams

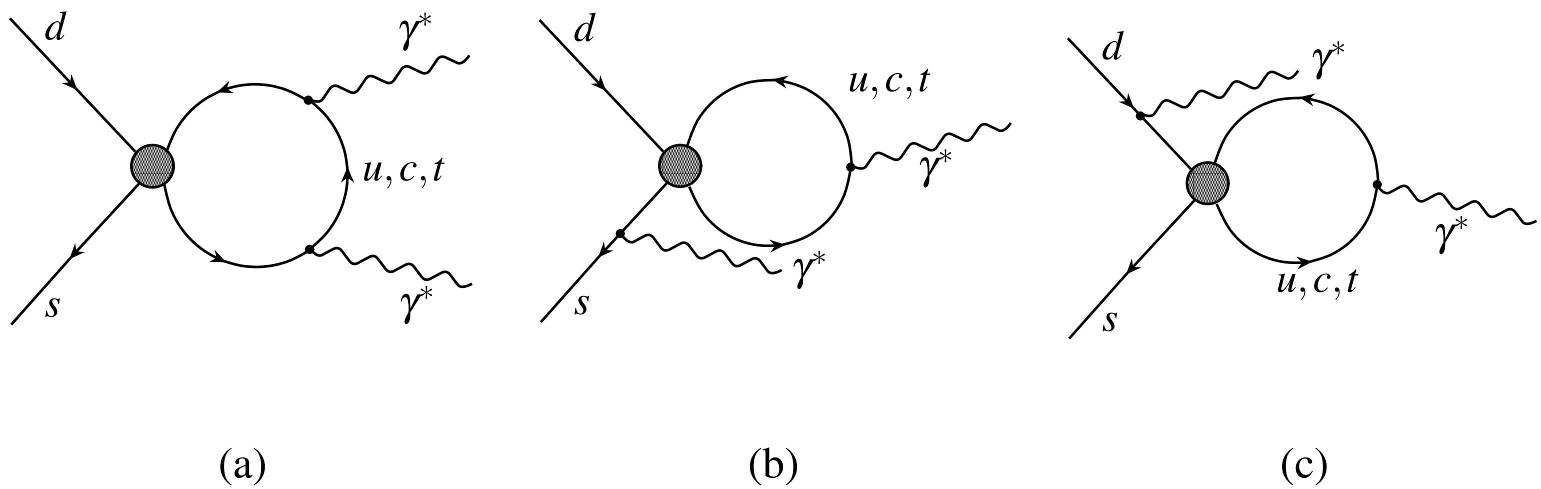

FIG. 13: Lowest order effective quark diagrams contributing to $K_L^0 \to \gamma^* \gamma^*$ in the framework of a perturbative QCD expansion of $F(q^2, q^2)$. [17]

Form Factors (QCD)

- QCD Form Factor:

$$f\left(q_1^2, q_2^2\right) = \frac{F\left(q_1^2, q_2^2\right)}{F\left(0,0\right)} = 1 + \alpha\left(\frac{q_1^2}{q_1^2 - m_V^2} + \frac{q_2^2}{q_2^2 - m_V^2}\right) + \beta\,\frac{q_1^2 q_2^2}{(q_1^2 - m_V^2)(q_2^2 - m_V^2)} \tag{39}$$

α is found from fits to B($K_L^0 \rightarrow \mu^+\mu^-\gamma$) and B($K_L^0 \rightarrow e^+e^-\gamma$).

β is found from B($K_L^0 \rightarrow \mu^+\mu^- e^+ e^-$).

The ρ meson is chosen to dominate the interaction,
$m_V = m_\rho \approx 770$ MeV/c^2

Form Factors (χPT)

- χPT Form Factor:

$$F_2(t,t') = \frac{\alpha_{em} C_8}{192\pi^3 F_\pi^3}\left[-(a_2+2a_4)D(t,t',m_V) + C(\mu)(t+t')\right] \qquad (40)$$

Where the momentum dependence is carried by $D(t,t',\mu)$:

$$\begin{aligned} D(t,t',m_V) = (t+t')\left[\frac{10}{3} - \left(\ln\frac{M_K^2}{m_V^2} + \ln\frac{M_\pi^2}{m_V^2}\right)\right] + \\ 4\left[F(M_\pi^2,t) + F(M_K^2,t) + F(M_\pi^2,t') + F(M_K^2,t')\right] \end{aligned} \qquad (41)$$

where

$$F(m^2,t) = \left(\left(1-\frac{y}{4}\right)\sqrt{\frac{y-4}{y}}\ \ln\frac{\sqrt{y-4}+\sqrt{y}}{\sqrt{y-4}-\sqrt{y}} - 2\right)m^2 \qquad (42)$$

Part III

$K_L^0 \rightarrow \mu^+\mu^-e^+e^-$ at E871

Motivation for $K_L^0 \to \mu^+\mu^-e^+e^-$ at E871

- E871 was designed to measure ultra rare dilepton decays
- The $\mu\mu$ data set yielded 6216 candidate events for $K_L^0 \to \mu^+\mu^-$
- Single event sensitivity for $\mu\mu$ was 1.15×10^{-12}
- Measured B($K_L^0 \to \mu^+\mu^-$)=7.18×10^{-9}.

Weak dispersive amplitude ($\mathscr{A}_{SD}$) was computed by subtracting the unitary bound and an *estimate* of the $|Re(\mathscr{A}_{LD})|$ as computed by Ambrosio [17].

$\mathscr{A}_{LD}$ is model dependent! Relies on knowledge of $F(q^2, q'^2)$ and parameters from VDM, QCD, χPT, etc...

Need to measure in a self consistent manner $K_L^0 \to \ell^+\ell^-\ell^+\ell^-$

Want to have (roughly) the same systematics as the $K_L^0 \to \mu^+\mu^-$ measurement.

$K_L^0 \to e^+e^-e^+e^-$ was observed as a background in the $K_L^0 \to e^+e^-$ analysis, but final state is not distinct. Has in interference terms and other physics backgrounds which make it impractical to measure.

Solution:

Measure $K_L^0 \to \mu^+\mu^-e^+e^-$!

Properties of $K_L^0 \to \mu^+\mu^- e^+ e^-$

- Totally distinct final state (no interference terms)
- Form factors result in enhancement of high mass signal
- Form factors soften the e^+e^-pair
- Kinematics similar enough to $K_L^0 \to \mu^+\mu^-$ to provide events in the $\mu\mu$ data set
- Directly accesses $\mathscr{A}_{LD}$
- Might distinguish between $F(q^2, q'^2)$ models

Prior Measurements

At the inception of the search for $K_L^0 \to \mu^+\mu^-e^+e^-$ in the E871 data set, there was one observed event[5].

Fermilab Experiment E799 measured:

$$\Gamma(\mu^+\mu^-e^+e^-)/\Gamma_{total} = 2.9^{+6.7}_{-2.4} \times 10^{-9}, \tag{43}$$

- This result spanned almost a full order of magnitude in it's uncertainty.
- No differentiation between form factor models.
- Extraction of $K_{\gamma^*\gamma^*}$ vertex and $\mathscr{A}_{LD}$ suffer uncertainties.

During the analysis, 43 additional events were reported by the KTeV collaboration[6], with branching ratio of 2.62×10^{-9}.

- Still no clear differentiation between models.

Event Signatures for E871

E871 is essentially a two-body spectrometer. E871 was originally designed to search for rare dileptonic decays of K_L^0 ($\mu\mu$,ee,μe).

- All events are mandated to have two fully reconstructed charged particle tracks of opposite polarity which fulfill the dilepton trigger.
- Primary tracks must satisfy tracking and parallelism requirements
- Primary tracks must reconstruct to an invariant mass $>$ 460MeV/c^2

Only the $\mu\mu$ data stream is appropriate for this reconstruction requirement.

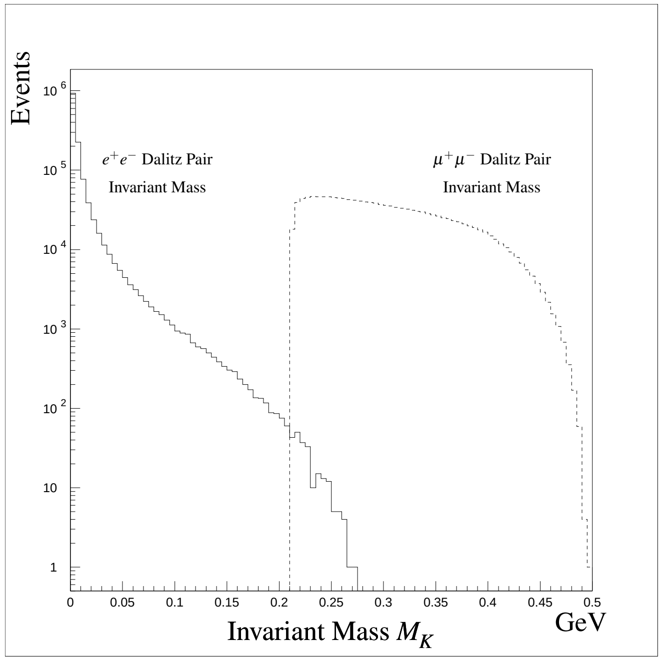

(a) Invariant mass reconstruction of e^+e^- and $\mu^+\mu^-$ pairs

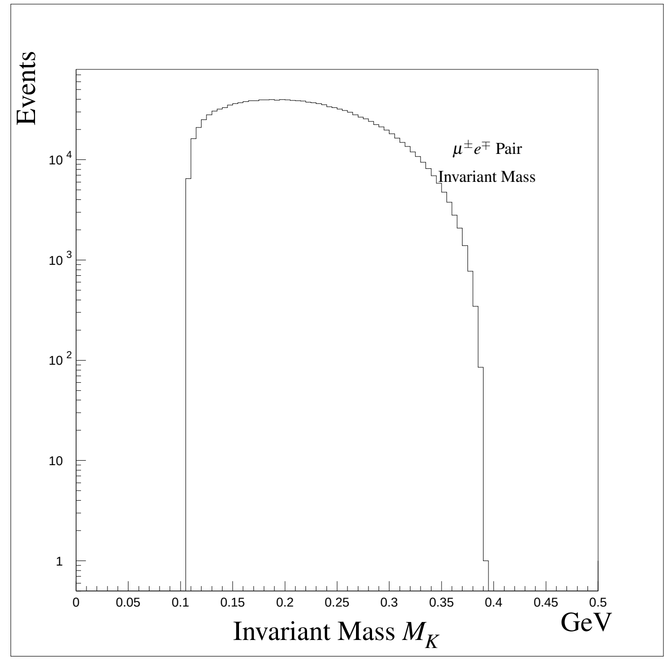

(b) Invariant mass reconstruction of $\mu^\pm e^\mp$ tracking pairs

FIG. 14: Invariant mass reconstructions for $K_L^0 \to \mu^+\mu^-e^+e^-$ using (a) (e^+e^-), $(\mu^+\mu^-)$ and (b) $(\mu^\pm e^\mp)$ tracking pairs

In addition to the $\mu^+\mu^-$ vertex reconstruction, the e^+e^-pair must register in the forward spectrometer.

The e^+e^-pair is *very soft* and may not fully traverse the spectrometer.The signature is broken down as follows:

1. Full four track vertex reconstruction of $\mu^+\mu^-e^+e^-$ with invariant mass at M_{K_L} and low p_T^2.
2. Three track vertex reconstruction with one missing e^+ or e^- with invariant mass greater than $460MeV/c^2$.
3. Two track vertex reconstruction with invariant mass greater than $460MeV/c^2$ and two correlated e^+e^- tracking stubs projecting back to an associated $\mu^+\mu^-$ event vertex.
4. Two track vertex reconstruction with invariant mass greater than $460MeV/c^2$, and a single e^+ or e^- tracking stub projecting back to the primary $\mu^+\mu^-$ event vertex.

Partial Tracks (Stubs)

- The e^+e^- pairs are very soft and carry little of the available invariant mass and momentum even when boosted into the lab frame.
- The e^+e^- pairs have high angular correlation and small opening angle.
- In the first dipole magnet they experience a 416 MeV/c transverse (inbend/outbend) momentum kick.
- Low momentum particles can be ejected from the spectrometer, or bent across the beam line.
- These trajectories leave tracking information only in the first two straw drift chambers.

Tracking information from SDC1 and SDC2 are combined to form a partial track "stub"

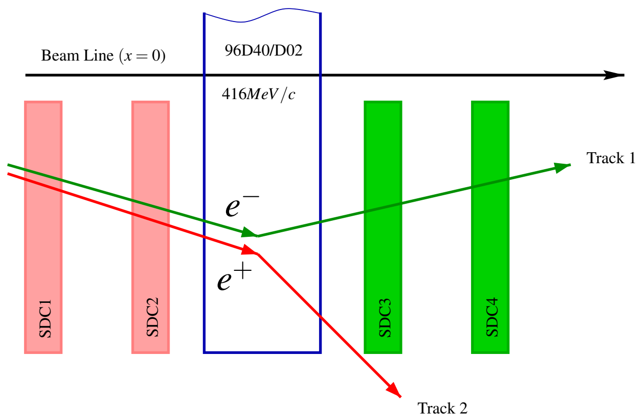

(a) Ejection of positron track from active spectrometer volume based on polarity mismatch with analyzing magnet 96D40/D02

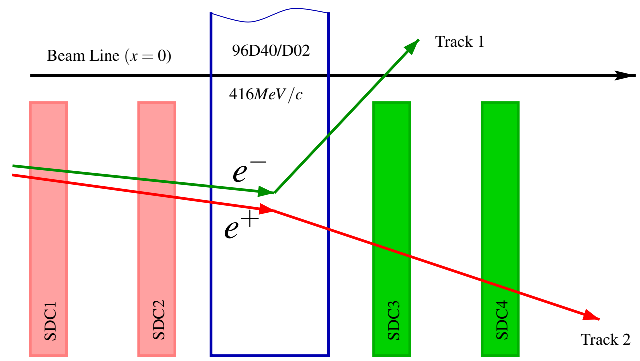

(b) Loss of particle tracking due to excessive inbend of extremely low momentum electron track

FIG. 15: Examples of low momentum e^+e^-Dalitz pair trajectories leaving partial (stub) tracks in straw drift chambers SDC1/SDC2

Background

The $K_L^0 \to \mu^+\mu^-e^+e^-$ event signal can be mimicked by other real physics events which undergo decays in flight, pair production, particle misidentification or multi-event pile-up.

In particular the following decay channels were examined:

- $K_L^0 \to \mu^+\mu^-\gamma$
- $K_L^0 \to \pi^+\pi^-\gamma$
- $K_L^0 \to \pi^+\pi^-\pi^0$
- $K_L^0 \to \pi^+\pi^-e^+e^-$
- K_{e3} and $K_{\mu 3}$ pile-up[a]

[a] semi-leptonic decays $K_L^0 \to \pi^{\pm}e^{\mp}\nu_e$ and $K_L^0 \to \pi^{\pm}\mu^{\mp}\nu_\mu$

$K_L^0 \to \mu^+\mu^-\gamma$ **Background**

Only $K_L^0 \to \mu^+\mu^-\gamma$ contributes to the real physics background.

Mimics the signal when γ converts to a e^+e^- pair forward of the second layer of the first straw drift chamber.

Background rate is dependent on photon energy:

Energy	Expected Background Events
10 MeV	< 0.01 events
100 MeV	< 0.03 events
1 GeV	< 0.04 events

TABLE 3: Expected background events of the form $K_L^0 \to \mu^+\mu^-\gamma$ including geometric acceptance weights for the E871 apparatus

Other Backgrounds

Other background channels are eliminated by choosing:

$$M_{K_{\mu\mu}} > 463.047 \text{ MeV/c}^2 \tag{44}$$

K_{e3} and $K_{\mu 3}$ pileup are still a problem.

- Difficult to model
- Pileup rate not known well
- End up just doing a background subtraction using sidebands

Part IV

E871 Experimental Apparatus

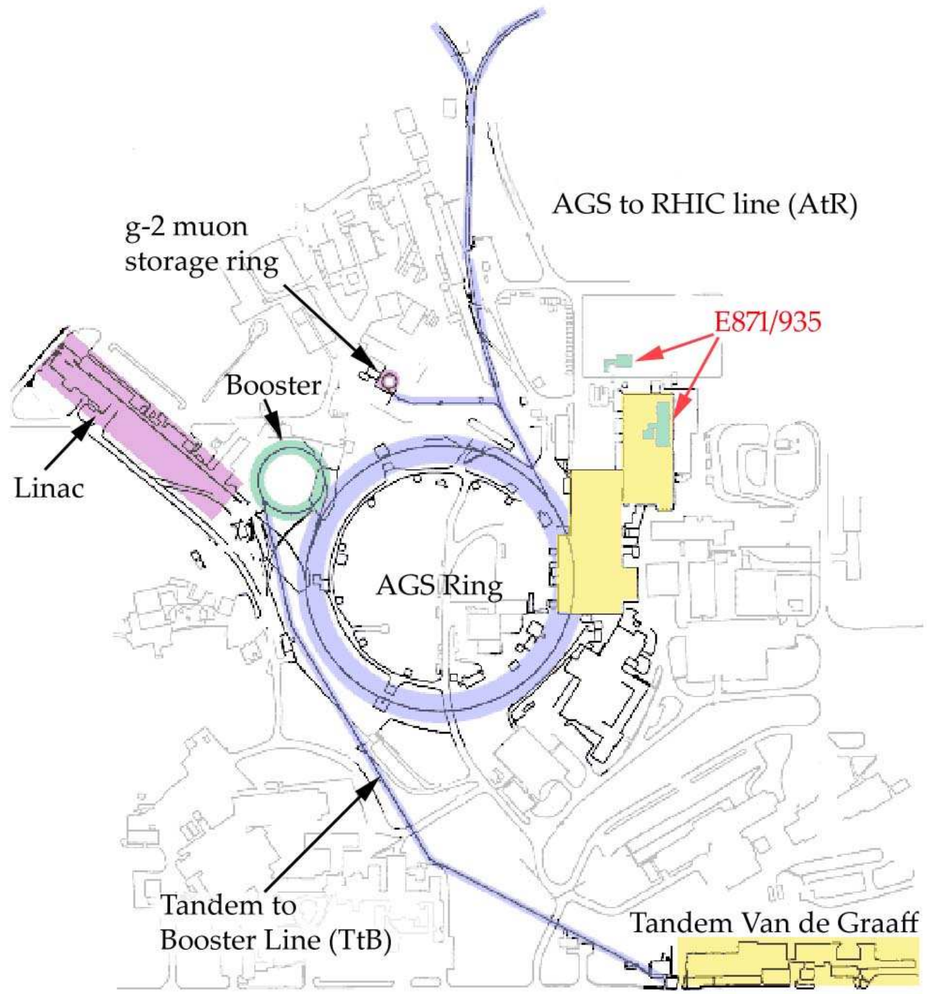

FIG. 16: Brookhaven National Labs AGS

E871 Detector System

- E871 was designed to reach a single event sensitivity of 10^{-12} (μe channel) over a 5600 hour run period at using the 24 GeV/c high intensity proton beam (15 Tp/spill)
- Experimental apparatus was assembled at BNL in the B5 secondary beam line of the AGS.
- Neutral beam stop was situated in the first analyzing magnet.
- Was upgraded in '97 to E935 (light $g\tilde{g}$ bound state search)

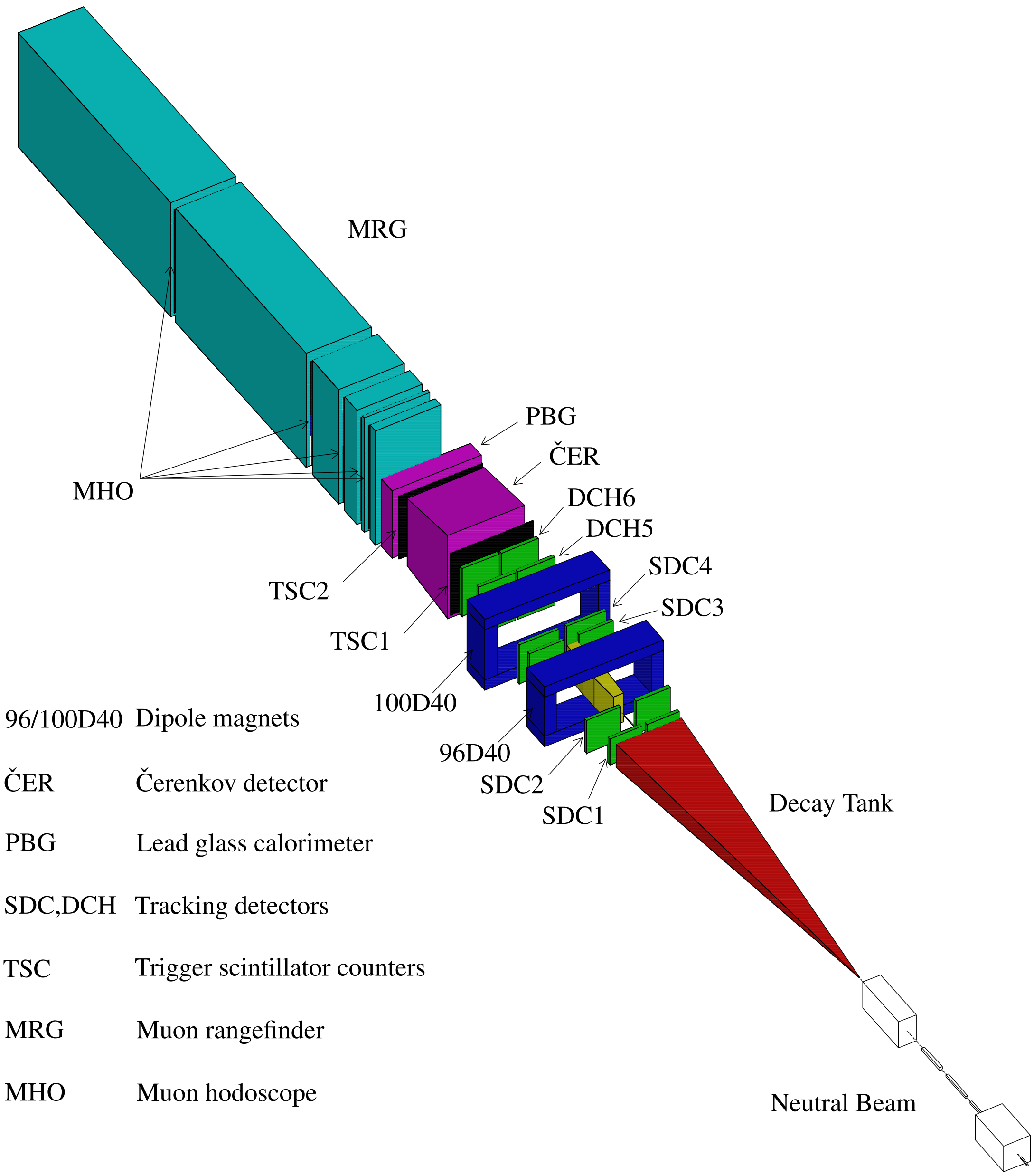

96/100D40	Dipole magnets
ČER	Čerenkov detector
PBG	Lead glass calorimeter
SDC,DCH	Tracking detectors
TSC	Trigger scintillator counters
MRG	Muon rangefinder
MHO	Muon hodoscope

FIG. 17: E871 Experimental apparatus

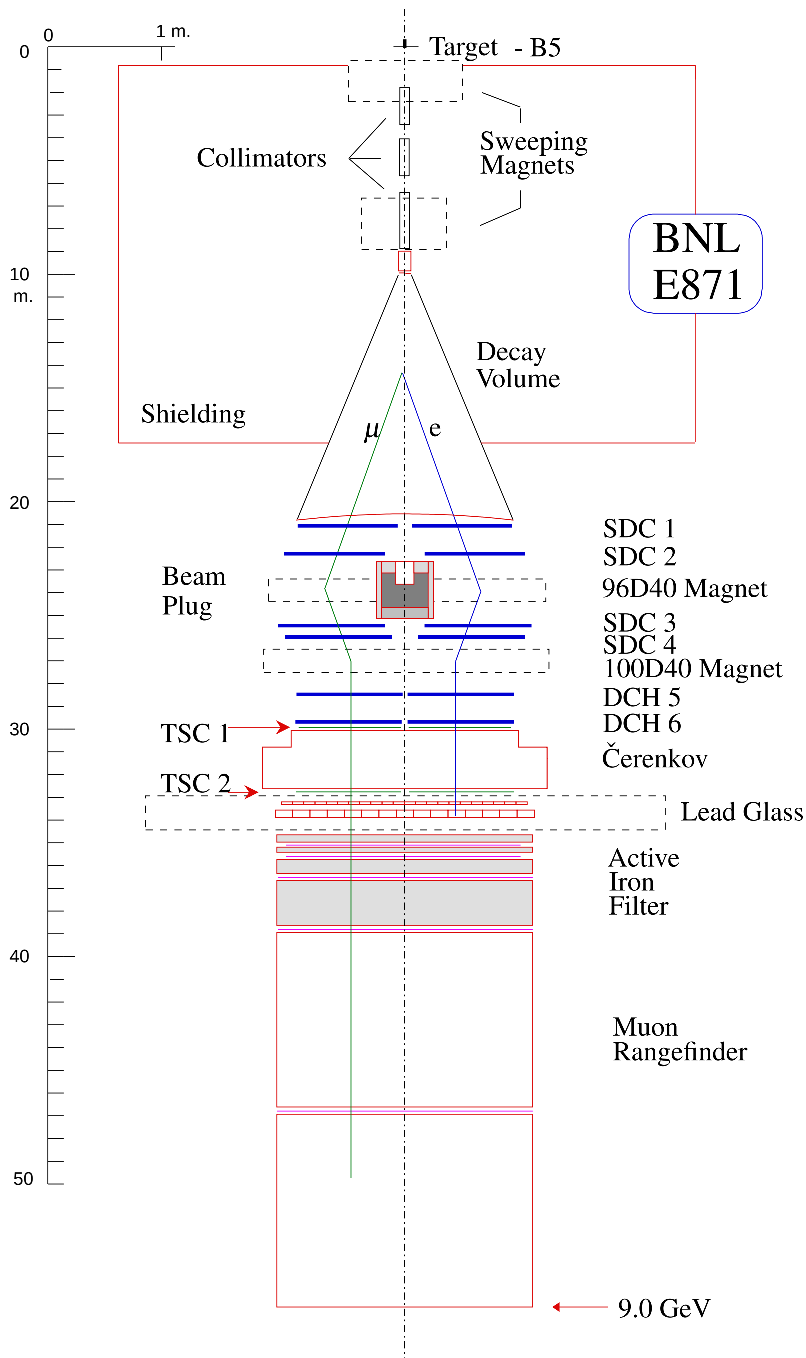

FIG. 18: E871 Spectrometer and particle identification

BNL AGS (B5 Line)

- AGS produces 24 GeV/c proton beam
- Total machine intensity peaks at 60 Tp
- Slow extraction creates a 1.5s spill
- Repetition rate from 3.2-3.8s
- Up to 25 Tp delivered to B5 target per spill
- Nominal B5 extraction set at 15 Tp

E871 Production Target

- Platinum target material 1.44 hadronic interaction lengths for the 24GeV proton beam
- Target was segmented for heat dissipation (5 segments 1995, 15 segments 1996)
- Target brazed [a] to a water cooled beryllium heat sink
- Mounted at 3.75° to the horizontal
- At incident target angle produces 2×10^8 kaons per spill
- Neutron to Kaon ratio $n : K^0 \approx 20$

[a] Ag-Cu-Sn alloy 1995, Ag-Cu-Li alloy 1996

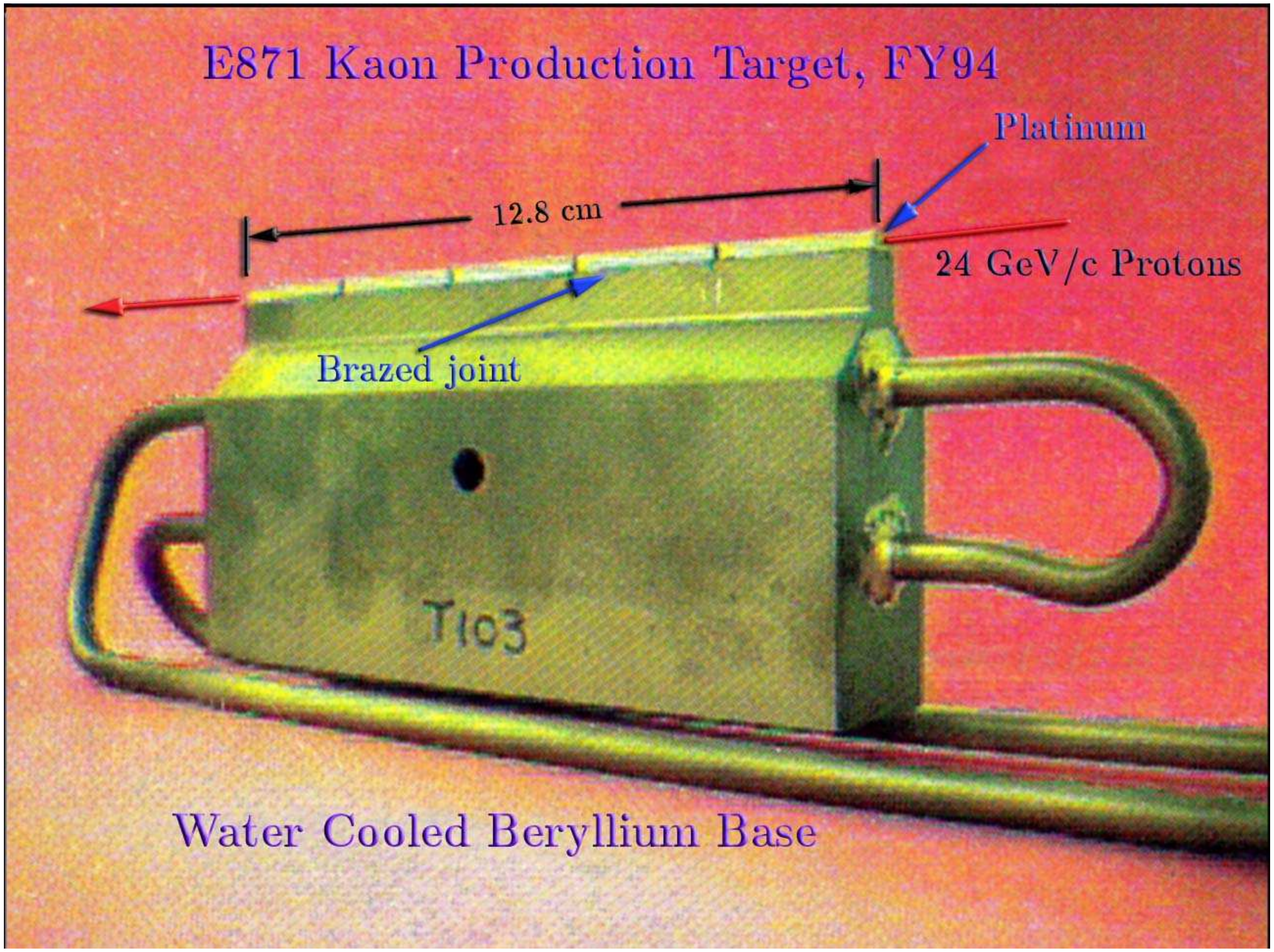

FIG. 19: E871 Production Target

E871 Forward Spectrometer

- Six sets of Left/Right symmetric tracking chambers
- Two high field dipole magnets provide two independent momentum measurements
- Trackers consist of 22 planes of x and y-view fast straw tubes wire chambers using 50/50 mixture CF_4 and ethane (SDC1-4)
- 100 μm/ns drift time.
- 800 kHz single channel hit rate in upstream chambers
- Over 6400 active straw tubes
- 8 planes of x and y-view hexagonal drift chambers (DCH5/6)
- 100 kHz single channel hit rate in downstream chambers

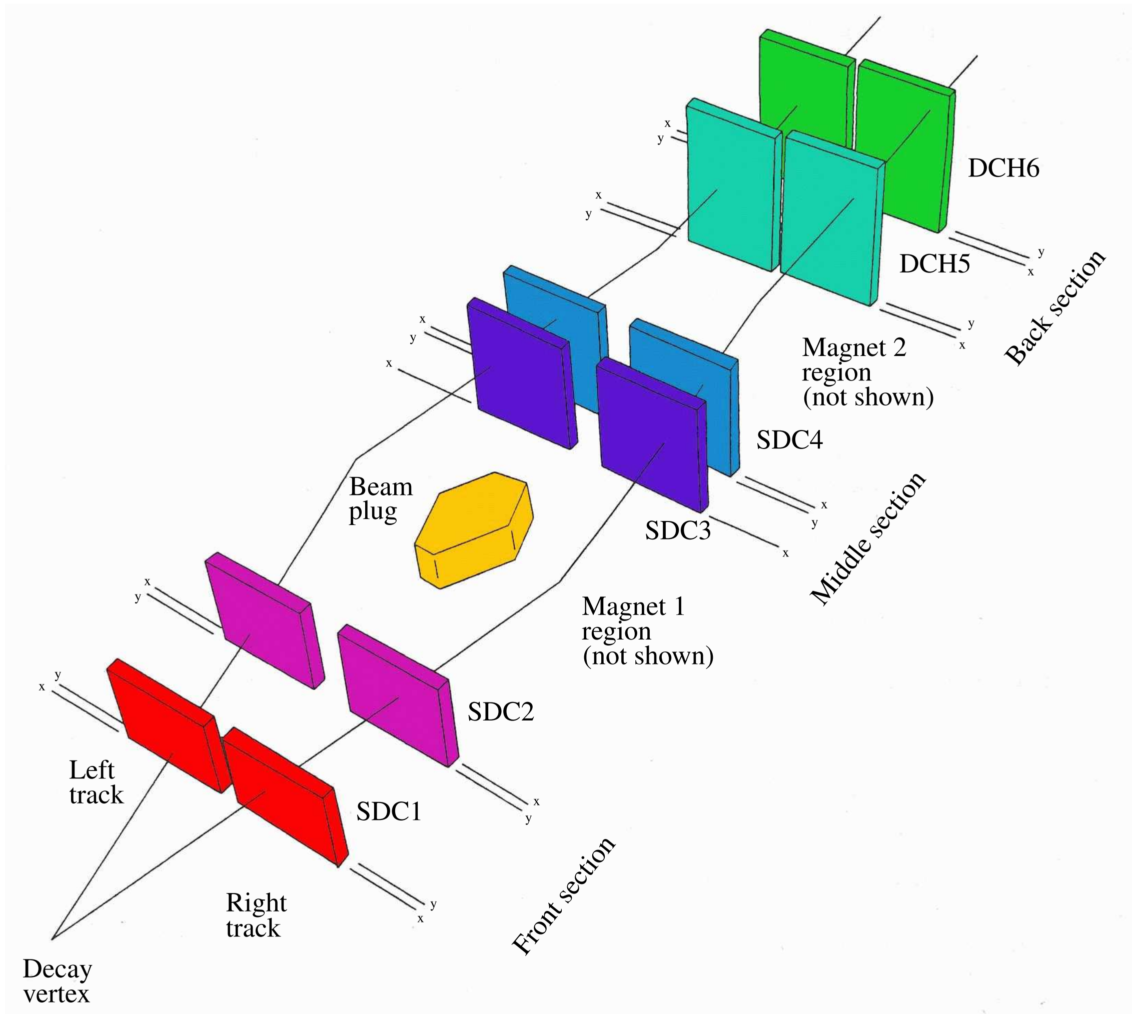

FIG. 20: E871 Spectrometer

Beam Stop

- Situated in the first magnet (96D40)
- Designed to stop a neutron flux $\sim 4 \times 10^9$ per spill
- 5000 kg of Tungsten-nickel alloy (Heavimet) and 1880 kg of copper
- Surrounding in borated polyethylene.

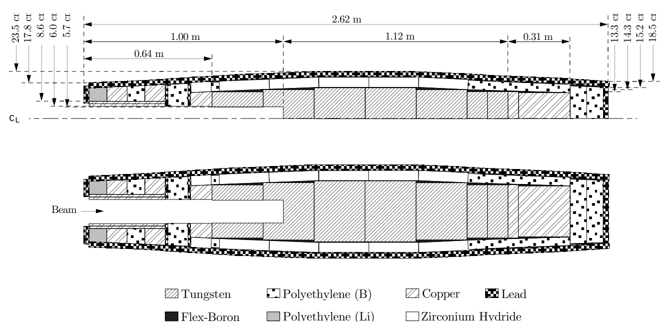

FIG. 21: Cross sectional view of E871 compact beam stop

Wire Chamber Rates

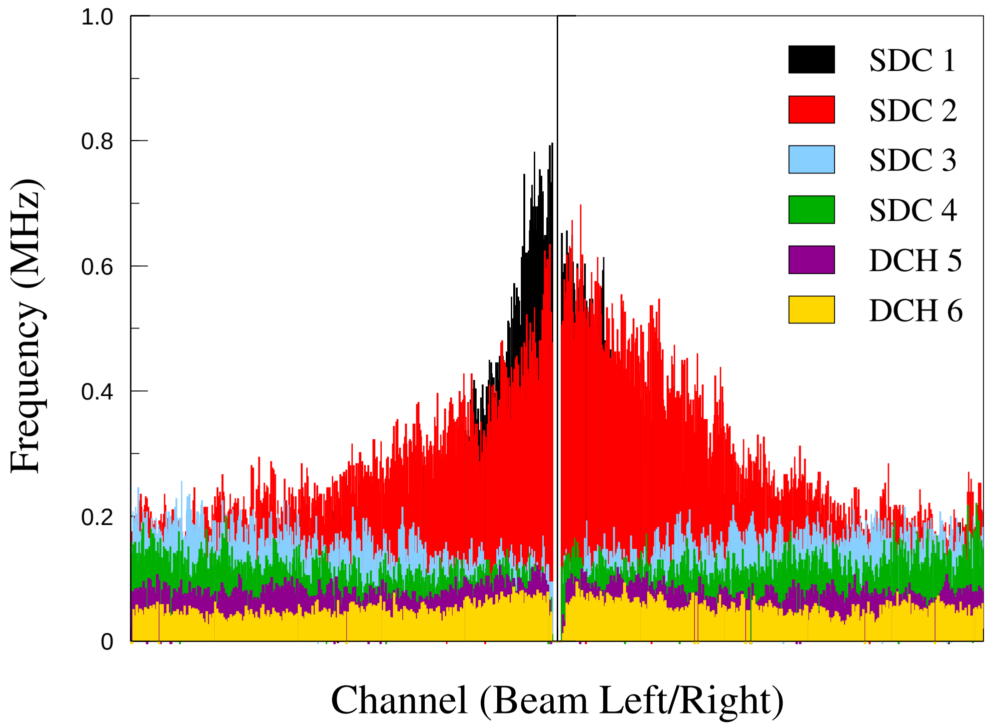

FIG. 22: Signal rate comparison between straw drift chambers and hexagonal drift chambers before and after the neutral beam stop

Trigger Scintillation Counters (TSC)

- Two banks of X measuring slats
- One bank of Y measuring slats
- Organic Scint. (Bicron BC-408)
- 2ns decay time, 430nm emission peak
- Served as L0/L1 Trigger system
- Imposes a "parallelism" requirement (± 2 slats)

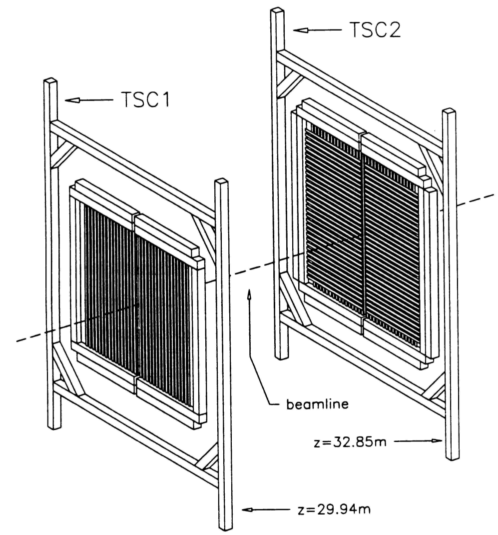

FIG. 23: TSC1/TSC2

Čerenkov Counter

First Particle ID detector – used for electron tagging

Used hydrogen gas (H_2) at a pressure of 7.6cm of water over atmosphere.

Particle	Threshold (GeV/c)	Particle	Threshold (GeV/c)
$e^{\pm}$	0.031	$\pi^{\pm}$	8.396
$\mu^{\pm}$	6.357	p	56.233

- Used Burle 8854 5inch phototubes.
- Run at positive high voltage (photocathode head at ground)
- Average single channel response of 5.6 photoelectrons.
- Detector efficiency was 98.6% for electron detection

H_2 Čerenkov Counter

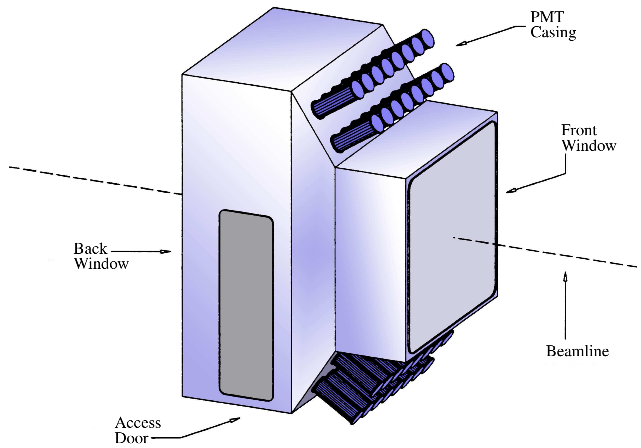

FIG. 24: E871 Čerenkov counter exterior geometry

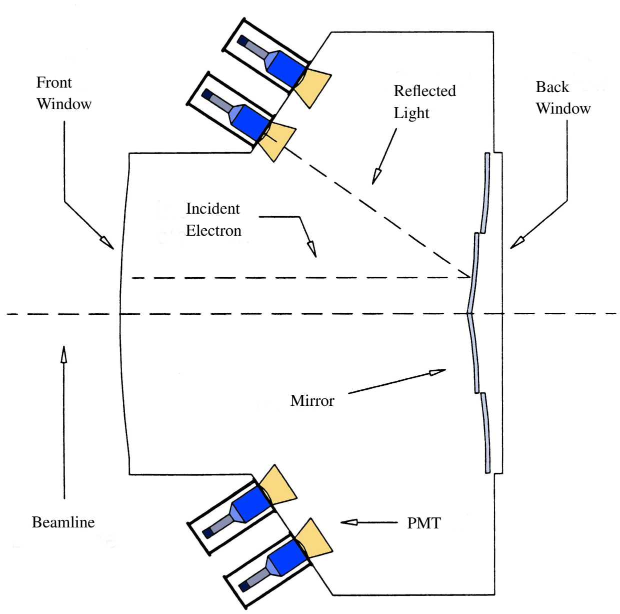

FIG. 25: E871 Čerenkov counter interior geometry

Lead Glass Array

Second Particle ID detector – used for electron/pion separation

- 6.4 tons of lead glass blocks in a light tight enclosure.
- Separated into forward (Convert) array and downstream (Absorber) array.
- 13.8 radiation lengths of material for E&M showers
- 1.6 hadronic interaction lengths
- E&M showers are initiated in the converter and fully absorbed in the back blocks.
- Hadronic showers have a low ratio of energy deposition between converter and absorber.

Lead Glass Array

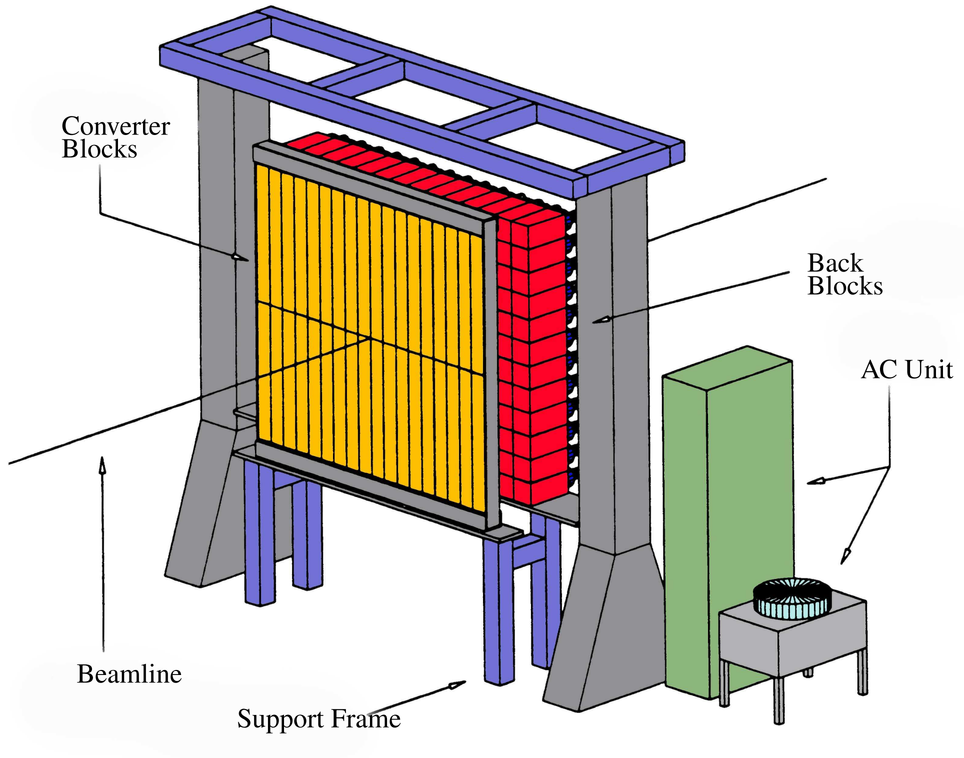

FIG. 26: E871 lead glass array with external cooling system

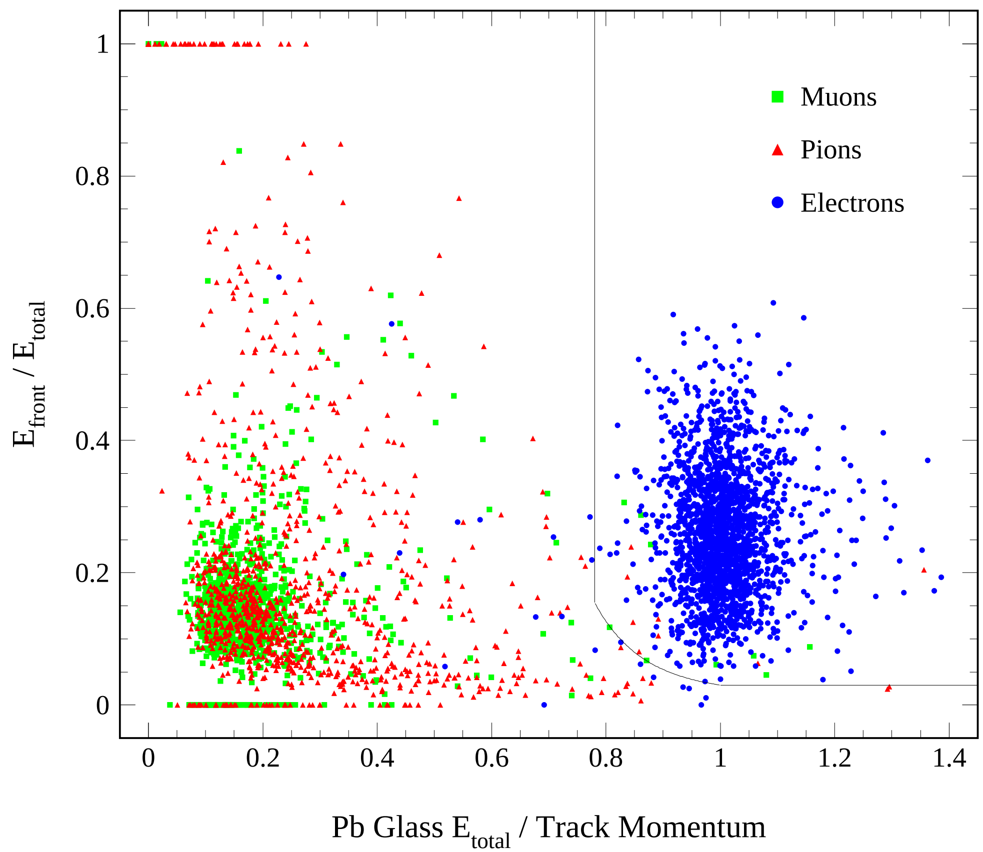

FIG. 27: Lead glass array electron/pion separation contour

Muon Range Stack

The muon range stack was a combination of two active detectors interspersed between blocks of iron, aluminum and marble.

- **Muon Hodoscope** Fast scintillator hodoscope
- **Muon Rangefinder** Wire proportional counters

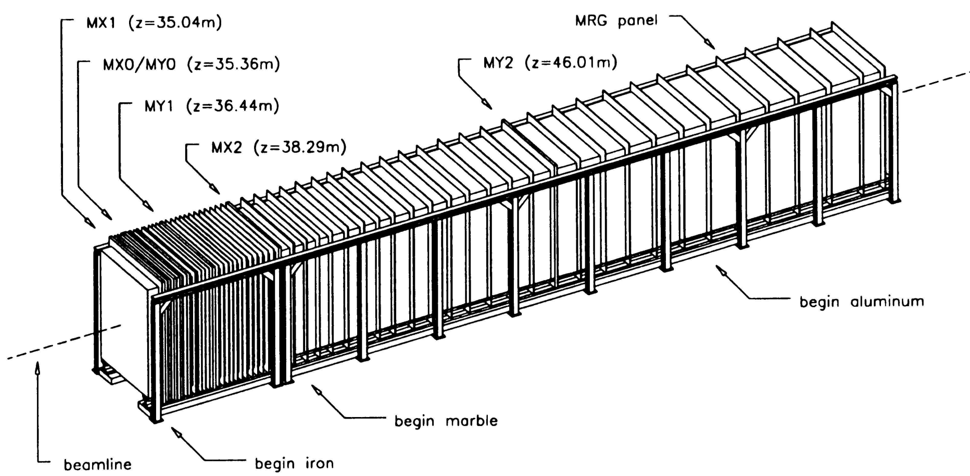

FIG. 28: E871 Muon ranger stack active detector placement

Muon Hodoscope (MHO)

Third particle ID detectors – Used for muon identification and triggering

- 6 X/Y scintillator/phototube panels
- X0/Y0 used as primary $\mu\mu$ trigger planes for L0/L1 trigger
- Trigger planes rebuilt for high rates

Muon Hodoscope Planes			
Plane	Momentum Gap (GeV/c)	Plane	Momentum Gap (GeV/c)
MX1	0.85	MY1	1.6
MX0	1.0	MX2	3.25
MY0	1.0	MY2	7.0

TABLE 4: MHO detector panel momentum gaps

Muon Hodoscope

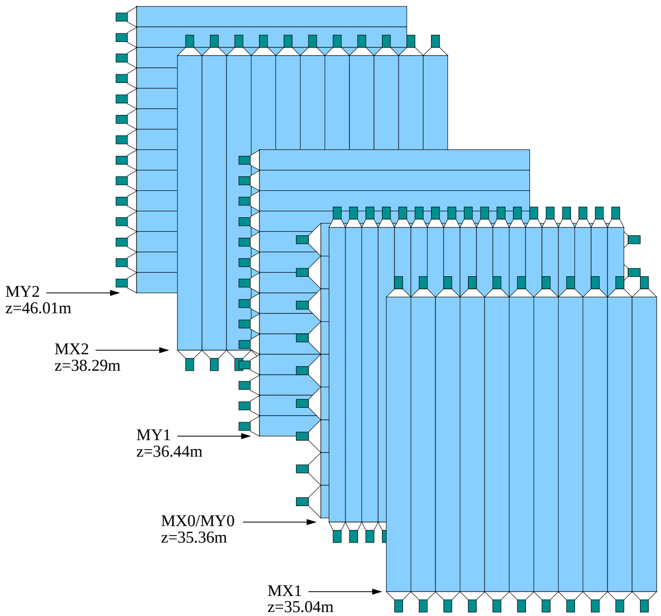

FIG. 29: Muon Hodoscope detector plane layout

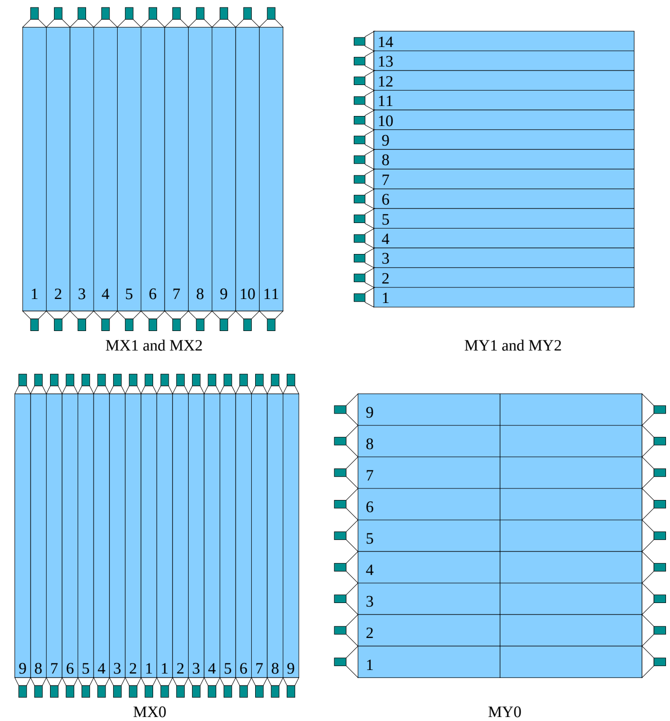

FIG. 30: Muon Hodoscope detector plane design

Muon Range Finder

Last particle ID detector – Separate muons from hadronic showers

- Argon/Ethane Wire proportional counters
- Used extruded aluminum honeycomb cells (192 or 256 wires per panel)
- 52 detector planes (X and Y measuring) 3×2.35m configs
- Spaced at 5% momentum gaps
- Measured out to maximum momentum of 10.258 GeV/c.
- Compared stopping point to measured spectrometer momentum.

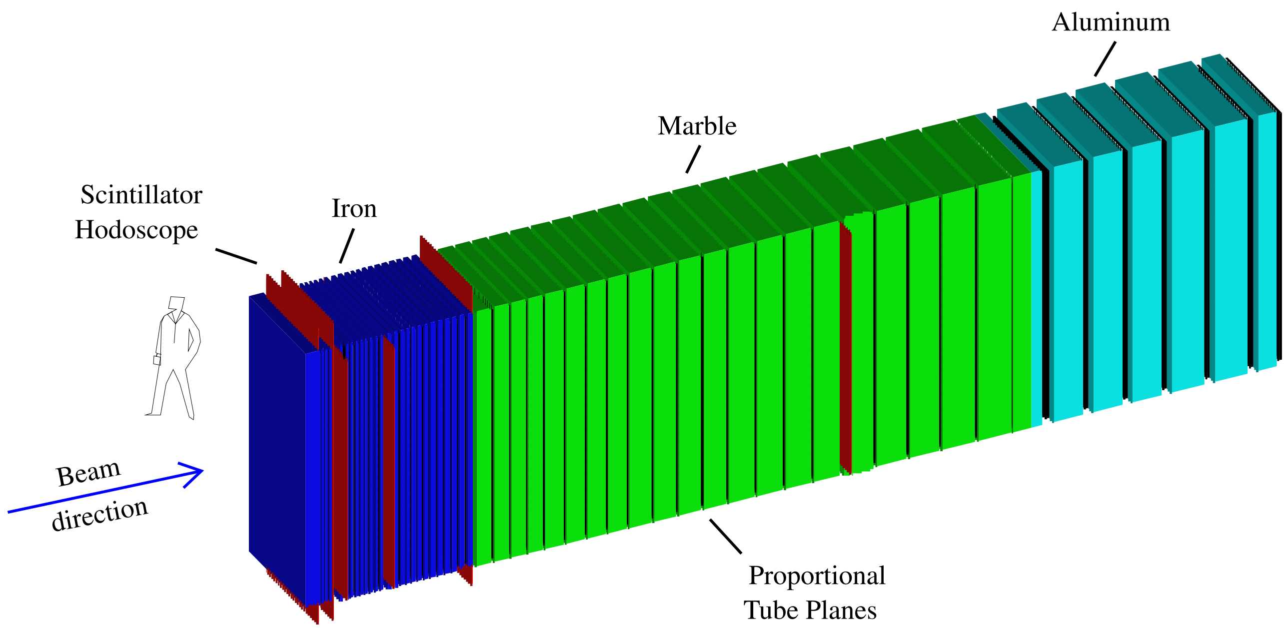

FIG. 31: E871 Muon range finder (MRG)

Triggering and DAQ

E871 involved a three stage triggering system designed to filter event data from an incident event rate of 10^6Hz down to 10^2Hz for output to tape.

- **Level 0** – Hardware trigger. Imposed only TSC tracking and parallelism.
- **Level 1** – Hardware trigger. Imposed rough particle ID.
- **Level 3** – Software trigger. Imposed vertex reconstruction and pattern recognition.

Level 0	$> 10^6$Hz non-parallel, 250kHz parallel
Level 1	10kHz ($\mu\mu$, μe, $e\mu$, ee)
Level 3	$\sim$300 physics events per spill, $\approx$110Hz

Trigger Types

The L1 trigger used four *"types"* of particle labels

$$\mu = L0 \cdot DC \cdot MHO$$

$$e = L0 \cdot DC \cdot \check{C}er$$

$$\pi = L0 \cdot DC \cdot \overline{Cer} \cdot \overline{MHO}$$

$$MB = L0 \cdot DC \qquad \text{(min-bias)}$$

These define 6 Left/Right physics triggers

Trigger Bit	Type	Trigger Bit	Type
1	$e \cdot \mu$	4	$\mu \cdot \mu$
2	$\mu \cdot e$	5	$MB \cdot MB$
3	$e \cdot e$	8	$L0 \cdot L0$

Example Trigger

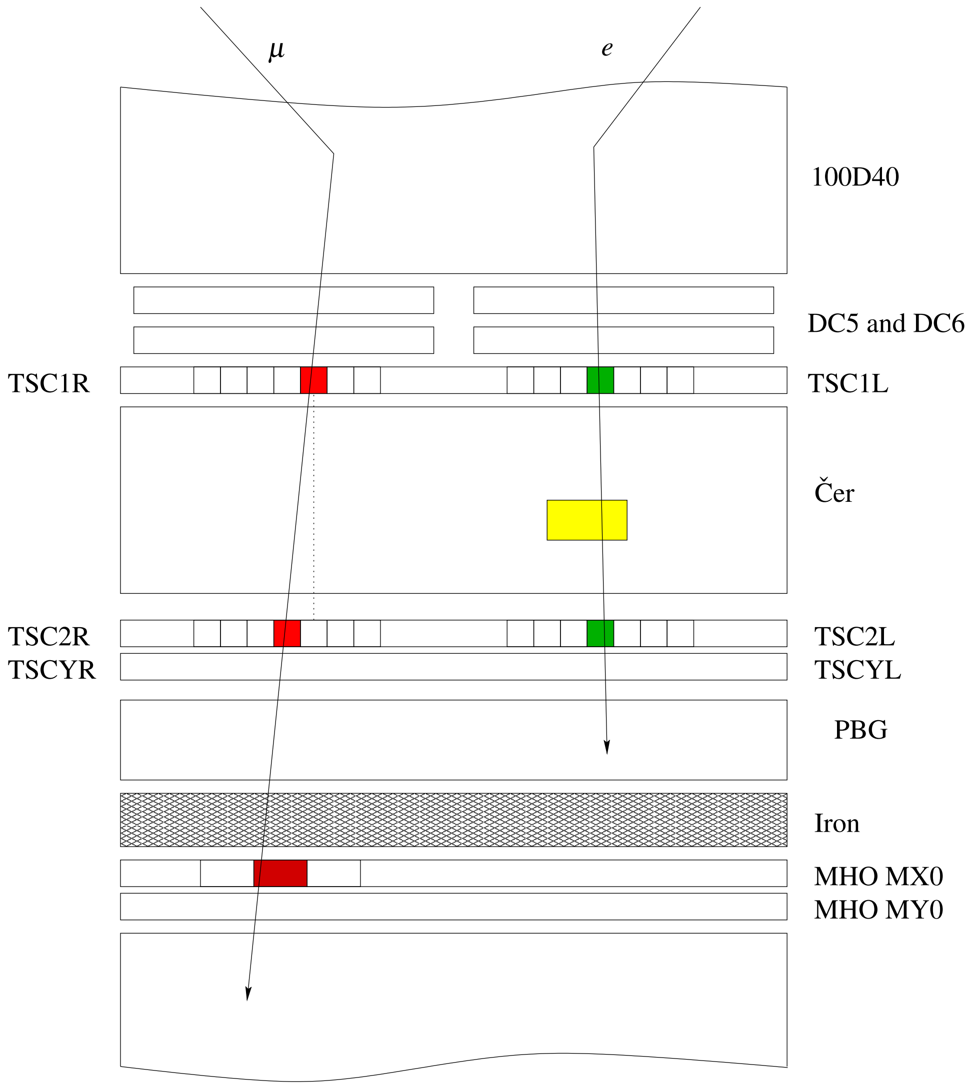

FIG. 32: Schematic overview of a level 1 event trigger

Part V

Monte Carlo Modeling

Monte Carlo Systems

The $K_L^0 \to \mu^+\mu^-e^+e^-$ analysis used two different and distinct types of Monte Carlo models to simulate the detector apparatus and kaon decay kinematics.

- **Geant Model** – Used for superior particle transport and examination of decay kinematics and distributions outside of sensitive volumes.
- **E871 Simulation** – Used for full detector response and reconstruction efficiencies. Functions as a front end to the actual E871 analysis code.

Blind Analysis

The $K_L^0 \to \mu^+\mu^-e^+e^-$ analysis and Monte Carlo conformed to a series of "blinds" designed to prevent bias in the modeling, reconstruction algorithms and data cuts that were applied.

Blinding consisted of:

- **Monte Carlo Prescale** – All models received a blind prescale shifting the event generation parameters by up to $\pm 50\%$. These values were recorded for normalizations but not immediately available.
- **Primary Signal Region Blind** – The primary signal region in invariant mass $M_{K_{\mu\mu}}$ and p_t^2 was blacked out.
- **Secondary Signal Region Blind** – The secondary signal box using additional collinearity reconstruct was blacked out.

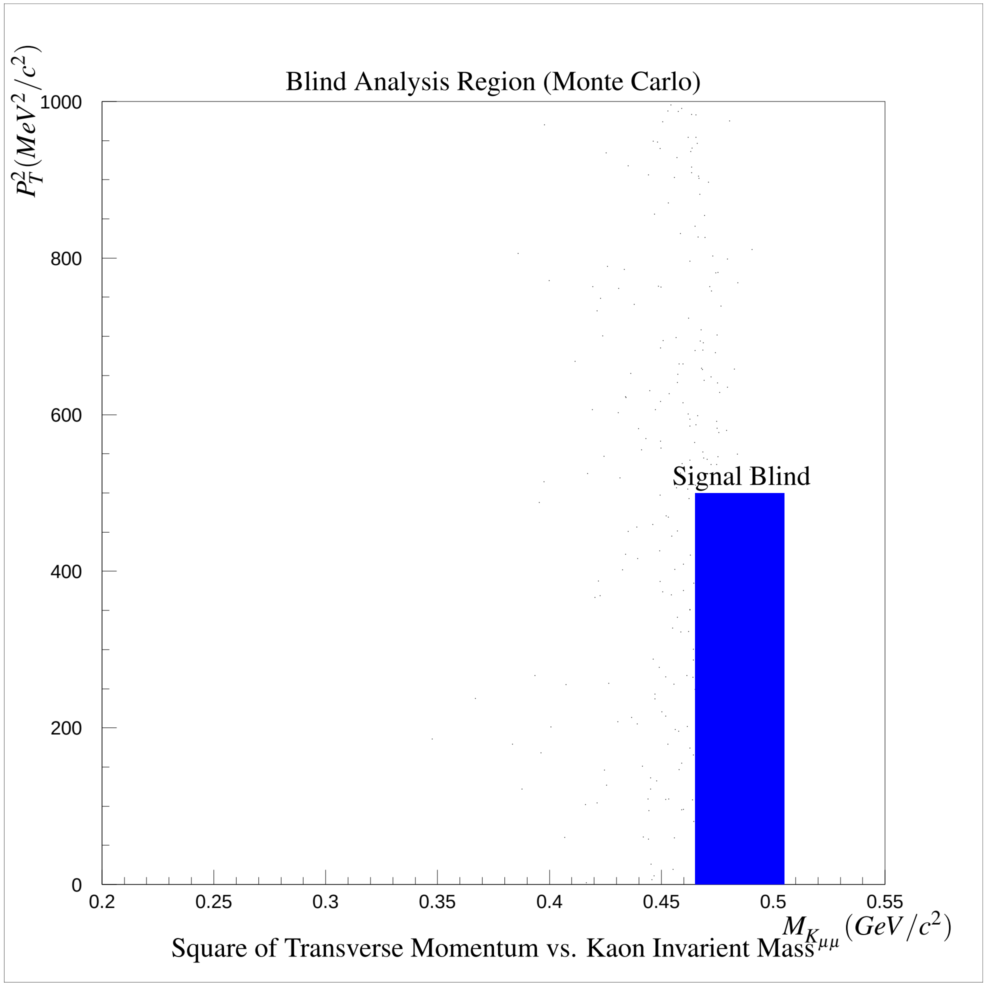

FIG. 33: Signal region blackout for development of threshold cuts and algorithm development under the blind analysis

Kaon Characteristics

The Monte Carlos need to correctly generate the K_L^0 spectrum and decay modes to be useful (this includes regeneration, oscillations, decay form factors etc...)

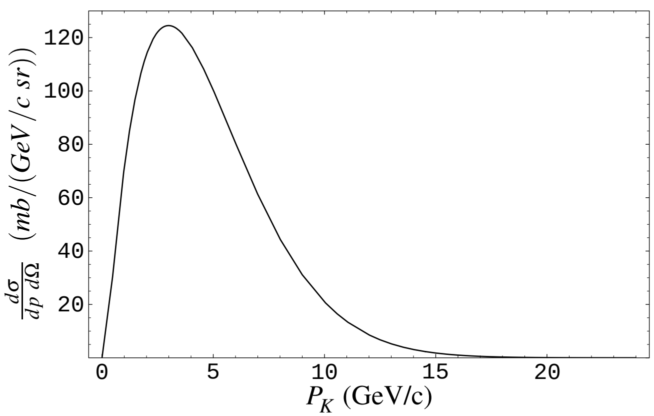

FIG. 34: K_L^0 production cross section at -3.75°

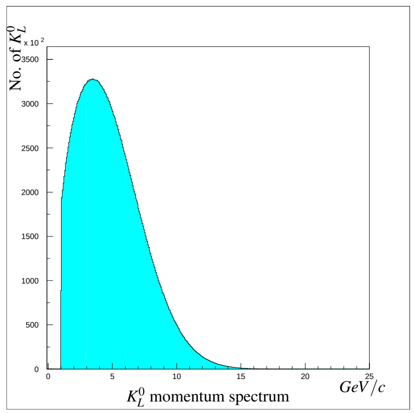

FIG. 35: Monte Carlo K_L^0 momentum spectrum[18]

Event Characteristics

Just some of the event characteristics that were examined in Monte Carlo:

- Primary/Secondary decay plane correlation
- Electron/Positron lab frame angular correlation
- Electron/Positron momentum spectra
- Electron/Positron transverse momenta
- Multiple Coulomb Scattering and e^-/e^+ opening angle
- Pair production and e^-/e^+ opening angle

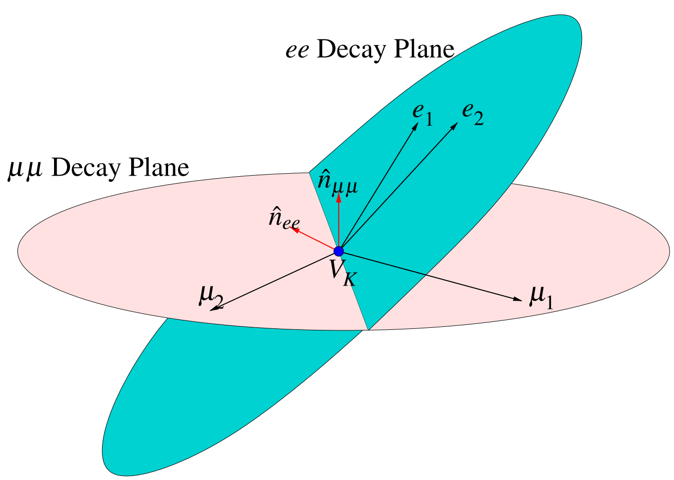

FIG. 36: Decay planes as defined by the event vertex and particle momenta p_{ℓ_i}

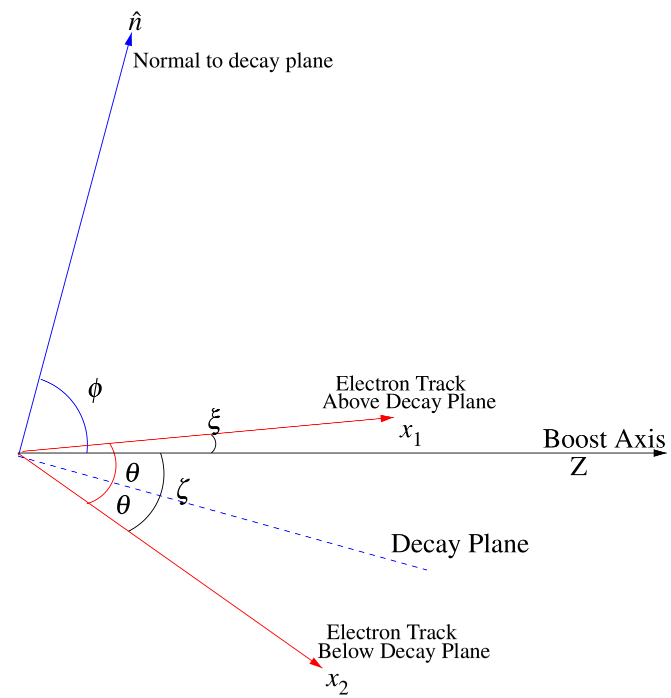

FIG. 37: Electron/Positron boost and decay plane geometry

Background Calculations

Monte Carlo simulations were used to investigate different sources of background.

- $K_L^0 \to \mu^+\mu^-\gamma$ background
- Includes form factors (χPT and Pseduoscalar meson exchange)
- Pair production included
- Pile up of K_{e3} and $K_{\mu 3}$

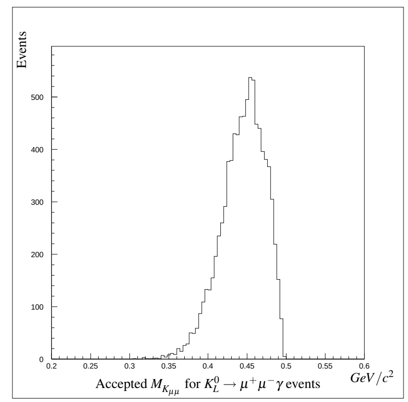

FIG. 38: Invariant mass reconstructions for $K_L^0 \to \mu^+\mu^-\gamma$

Monte Carlo Form Factors

To model the decay $K_L^0 \to \mu^+\mu^- e^+ e^-$ requires proper treatment of the decay of the pseudoscalar meson into a four lepton final state.

In addition model dependent form factors and the effects they have on the weighting of the final state particles distributions must be included.

This is not trivial!

We modeled:

- QED on-shell Kinematic [19]
- VDM with fits to $\mu\mu\gamma$ [20]
- QCD with sum rules for α and β [17]
- χPT with multiple parameter sets [21]

QED 4-Body Kinematic Phase Space

At the most basic level we model $K_L^0 \to \mu^+\mu^-e^+e^-$ as a straight 4-Body decay of a pseudoscalar.

The general form factor $f(q_1^2,q_2^2)/f(0,0)$ is taken to be purely on shell.

$$|\frac{f(q_1^2,q_2^2)}{f(0,0)}|^2 \sim 1 \tag{45}$$

With a non-trivial change of variable the differential decay amplitude becomes:

$$\Gamma = \frac{1}{\pi}\left(\frac{\alpha}{4\pi}\right)^2 \int\cdots\int dx_1 dx_2 dy_1 dy_2 d\phi \left|\frac{f(x_1^2,x_2^2)}{f(0,0)}\right|^2 \left[1-\frac{2(x_1^2+x_2^2)}{M_K^2}+\frac{(x_1^2-x_2^2)^2}{M_K^4}\right]^{3/2}$$
$$\times\left[\left[\frac{1}{x_1x_2}+\left(\frac{y_1^2}{x_1}+\frac{4m_e^2}{x_1^3}\right)\left(\frac{y_2^2}{x_2}+\frac{4m_\mu^2}{x_2^3}\right)\right]\sin^2\phi+\left[\frac{y_1^2+y_2^2}{x_1x_2}+\frac{4m_em_\mu(x_1^2+x_2^2)}{x_1^3x_2^3}\right]\cos^2\phi\right] \tag{46}$$

This is where most people stop.

Monte Carlo Form Factors

- VDM

$$F(s)_{VDM} = \alpha\sqrt{2}eG_F f_{K^*K\gamma}\left(\frac{m_\rho^2}{f_{K^*}f_\rho^2}\right)\left(1-\frac{s}{m_{K^*}^2}\right)^{-1} \times\left(\frac{4}{3}-\left(1-\frac{s}{m_\rho^2}\right)^{-1}-\frac{1}{9}\left[\left(1-\frac{s}{m_\omega^2}\right)^{-1}+2\left(1-\frac{s}{m_\phi^2}\right)^{-1}\right]\right) \tag{47}$$

- QCD

$$f_{QCD}\left(q_1^2,q_2^2\right)=\frac{F\left(q_1^2,q_2^2\right)}{F\left(0,0\right)}=1+\alpha\left(\frac{q_1^2}{q_1^2-m_\rho^2}+\frac{q_2^2}{q_2^2-m_\rho^2}\right)+\beta\frac{q_1^2q_2^2}{(q_1^2-m_\rho^2)(q_2^2-m_\rho^2)} \tag{48}$$

- χPT

$$F_{\chi PT}(q_1,q_2)=\frac{\alpha_{em}C_8}{192\pi^3F_\pi^3}\left[-(a_2+2a_4)D(q_1,q_2,M_\rho)+C(M_\rho)(q_1+q_2)\right] \tag{49}$$

Form Factor Enhancement

The form factors are momentum dependent. They alter the fundamental way in which the available energy and momentum is shared out between the final state particles.

- Both the QCD and χPT form factors lead to significant enhancement in the high $\mu\mu$ invariant mass region near M_K.
- Enhancement comes in the region to which E871 is most sensitive.
- Form factors soften the momentum spectrum of the e^-/e^+ pair. Results in greater forward angle acceptance and decay plane correlation.

The form factors greatly influence the geometric acceptance factor $A_{\mu\mu ee}$ used to calculate the normalization to the $K_L^0 \to \mu^+\mu^-$ data stream.

QCD Form Factor Enhancement

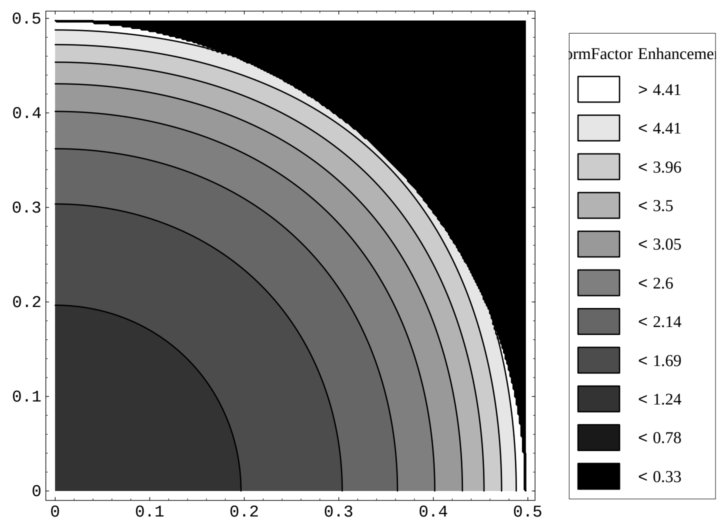

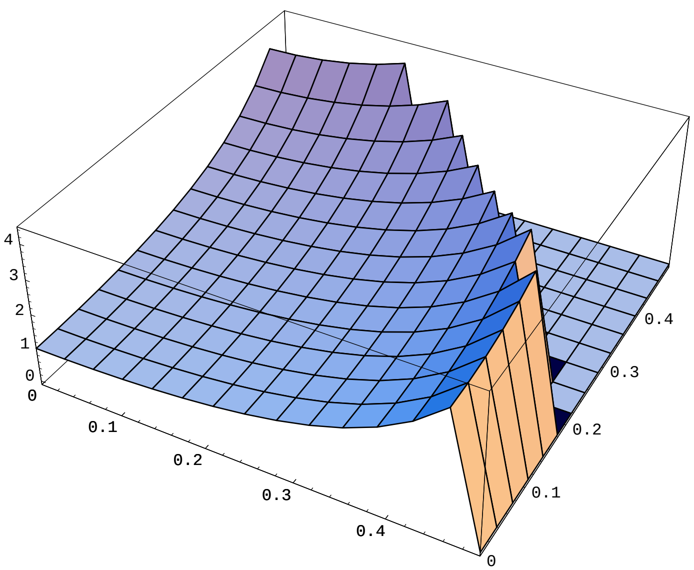

FIG. 39: QCD form factor [17] with high invariant mass enhancement bands.

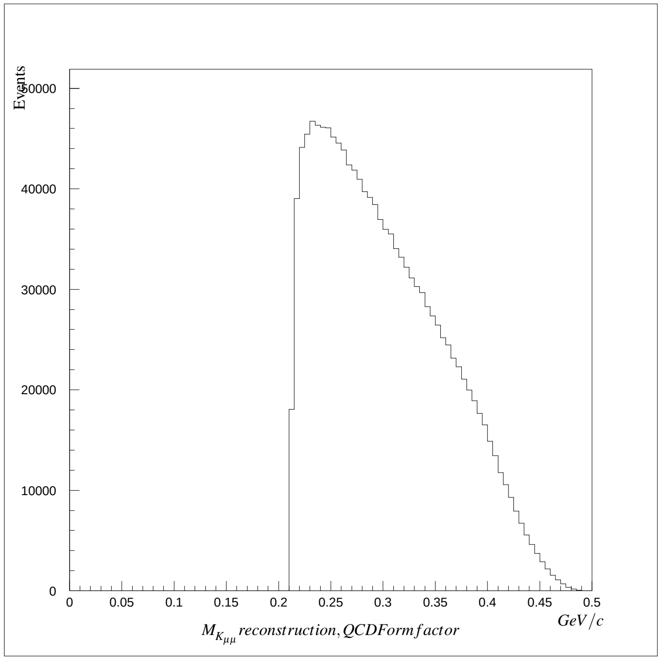

FIG. 40: $K_{\mu\mu}$ invariant mass spectrum with the QCD form factor

Model of the QCD form factor for $\beta = 2.56$ [17] used to simulate the decay $K_L^0 \rightarrow \mu^+\mu^-e^+e^-$. Kinematic restraints are placed upon the plot regions to show high mass enhancement of the decay near the kaon endpoint.

χPT Form Factor Enhancement

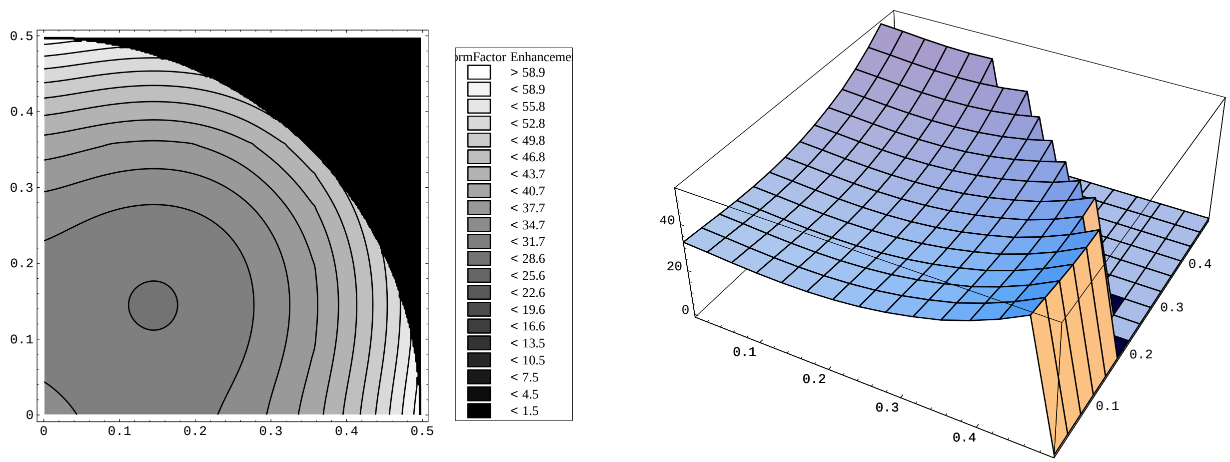

FIG. 41: Chiral form factor [21] with high invariant mass enhancement bands.

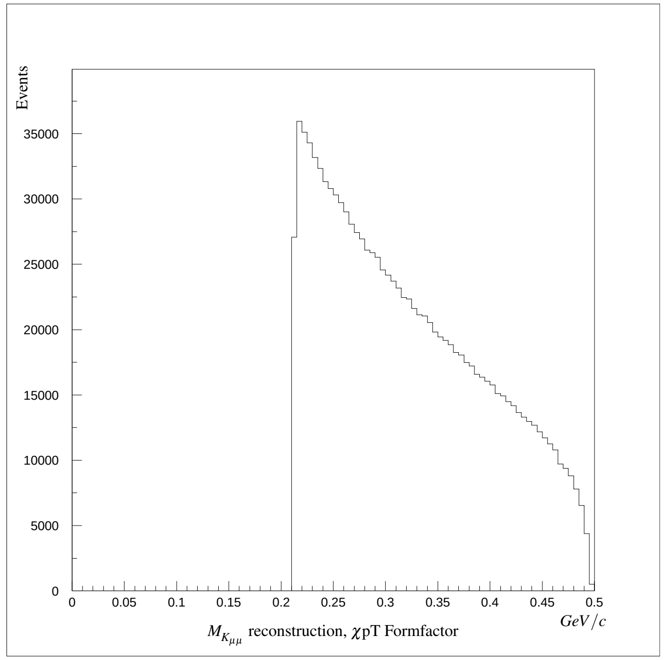

FIG. 42: $K_{\mu\mu}$ invariant mass spectrum with the Chiral form factor

Model of the Chiral form factor [21] used to simulate the decay $K_L^0 \to \mu^+\mu^- e^+e^-$. Kinematic restraints are placed upon the plot regions to show high mass enhancement of the decay near the kaon endpoint.

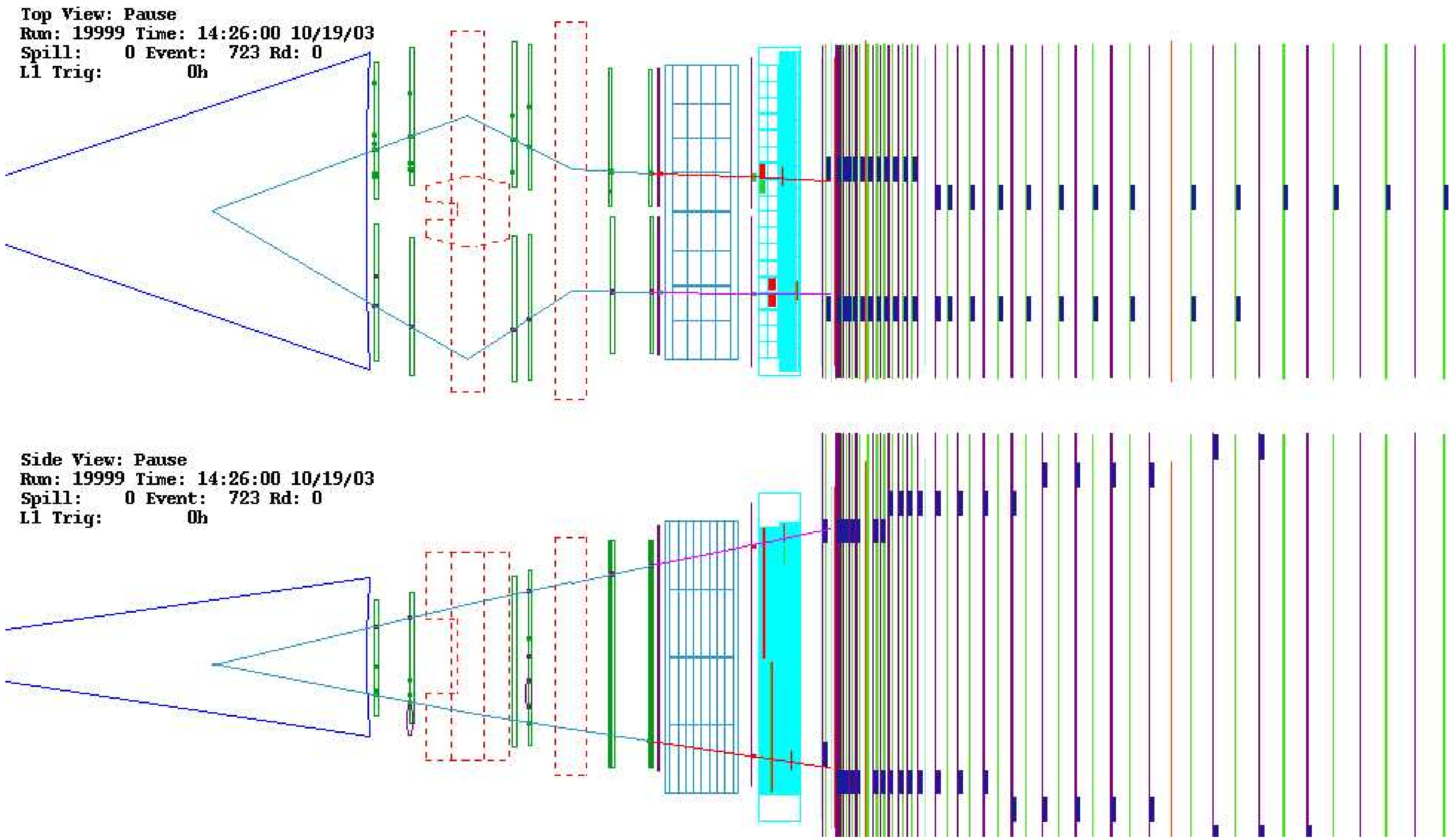

FIG. 43: Example $K_L^0 \to \mu^+\mu^-e^+e^-$ Monte Carlo event

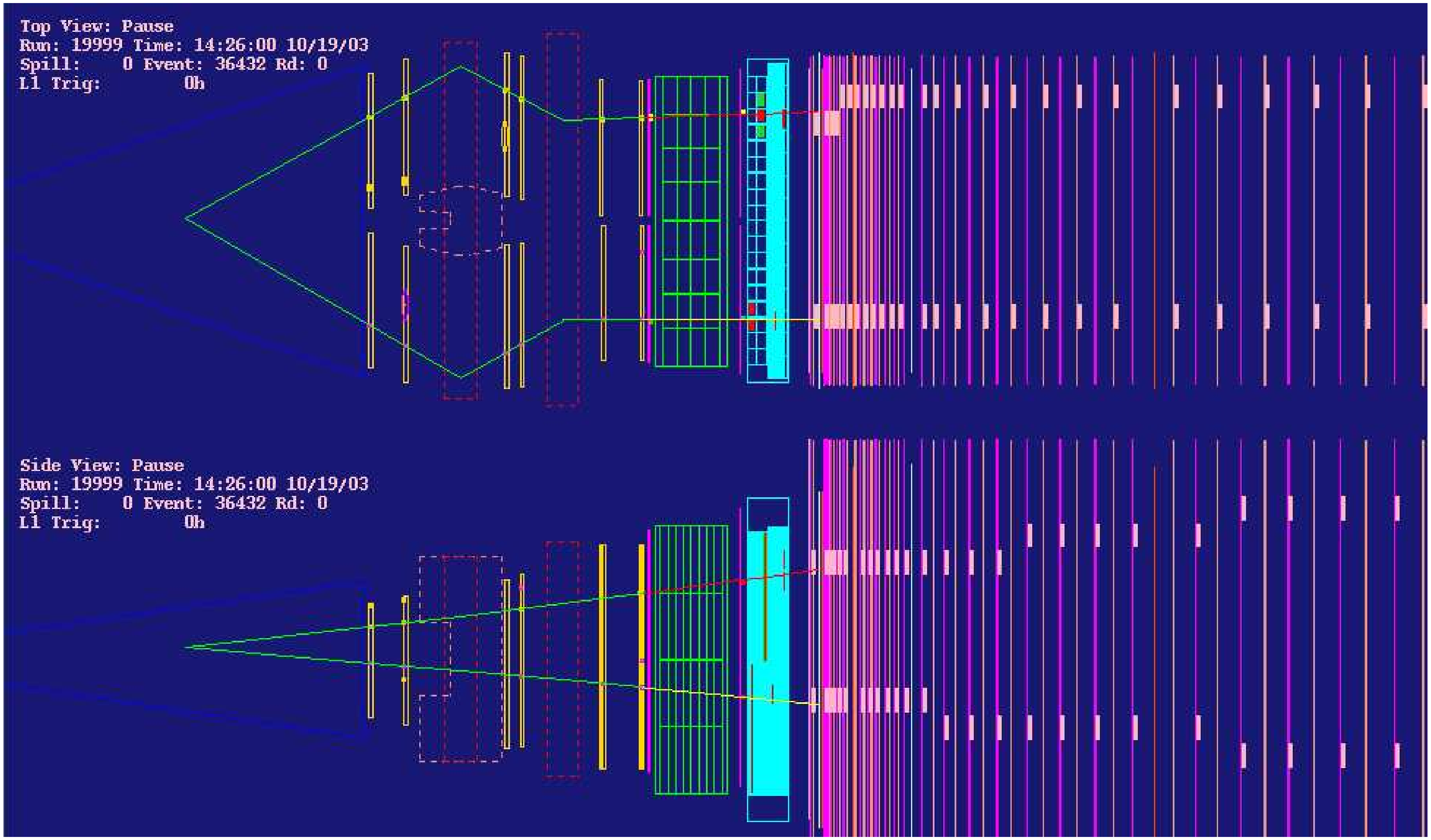

FIG. 44: Example $K_L^0 \rightarrow \mu^+\mu^-e^+e^-$ Monte Carlo event

Part VI

Analysis

Goals

The analysis for $K_L^0 \to \mu^+\mu^-e^+e^-$ is designed mirror the $K_L^0 \to \mu^+\mu^-$ analysis in order to to preserve the same systematics for each data stream.

- All primary $\mu\mu$ tracking and reconstruction cuts follow those of the production $\mu\mu$ analysis[1].
- Analysis focuses on identification of e^-/e^+ pairs and association of those pairs with the event vertex defined by $\mu\mu$ tracking.
- Cuts are designed to minimize acceptance loss to $\mu\mu$ and $\mu\mu ee$ events.
- Cuts are designed to provide a high certainty in identification of $K_L^0 \to \mu^+\mu^-e^+e^-$ events.

$\mu\mu$ Cut Differences

The $K_L^0 \to \mu^+\mu^-$ and $K_L^0 \to \mu^+\mu^-e^+e^-$ primary $\mu\mu$ track cuts differ only in that the $\mu\mu$ track reconstructions for $K_L^0 \to \mu^+\mu^-e^+e^-$ receive an explicit veto on the E871 signal box in kaon mass $M_{K_{\mu\mu}}$ and transverse momentum p_T.

- The veto prevents contamination of the $K_L^0 \to \mu^+\mu^-e^+e^-$ signal by $K_L^0 \to \mu^+\mu^-$ events.
- Contamination of the $K_L^0 \to \mu^+\mu^-$ signal by $K_L^0 \to \mu^+\mu^-e^+e^-$ events is calculated at a ratio of 1:57 from Monte Carlo.
- Total $K_L^0 \to \mu^+\mu^-e^+e^-$ contamination of the $K_L^0 \to \mu^+\mu^-$ signal peak is ≈ 2 events.

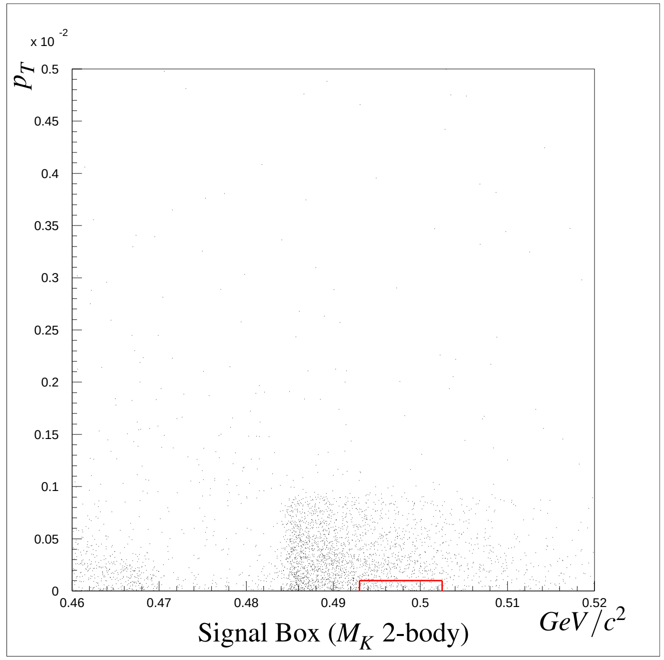

FIG. 45: $K_L^0 \to \mu^+\mu^-$ signal box. Region is explicitly vetoed for the $K_L^0 \to \mu^+\mu^-e^+e^-$ data stream

e^+e^- Track Finding (Basic)

Identification of the electron pairs is made using straw chamber hit clusters in SDC1 and SDC2.

Since the e^+e^-pairs are known to be extremely soft, only partial tracks (stubs) are searched for.

Basic method of stub finding:

- Search for all local hit clusters in SDC1/SDC2 in X and Y views
- Determine local track slopes for each hit cluster
- Perform X/X and Y/Y cluster matching to form segments
- Perform X/Y segment matching to form candidate stubs
- Check all possible ambiguities in matches for vertex DOCA
- Associate matches with $\mu\mu$ vertex.

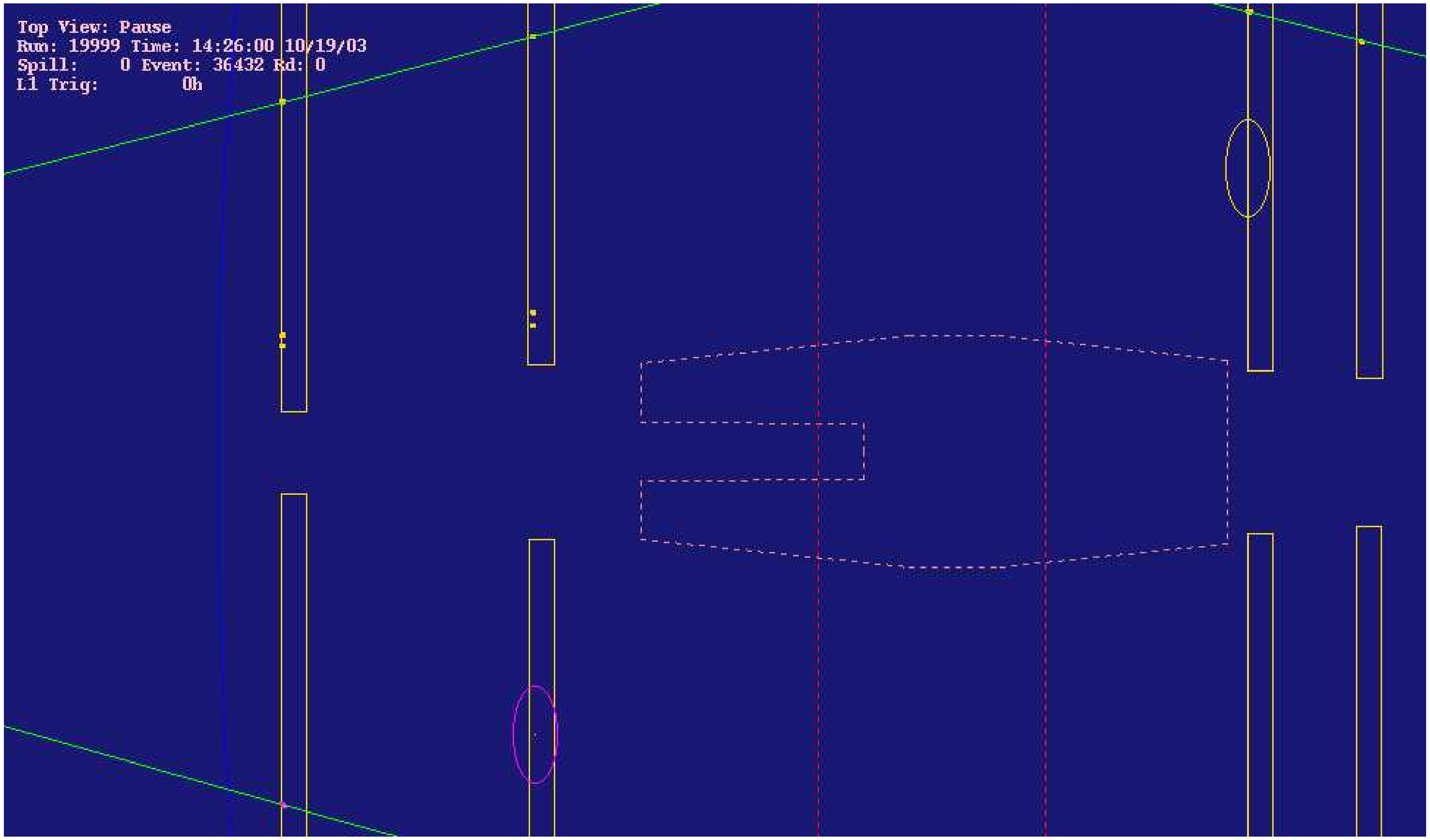
Top View: Pause
Run: 19999 Time: 14:26:00 10/19/03
Spill: 0 Event: 36432 Rd: 0
L1 Trig: 0h


E871 Event Display
Top View: Pause
Run: 19999 Time: 23:37:00 11/13/03
Spill: 0 Event: 723 Rd: 1
L1 Trig: 0h
Primary Track
SDC2 Hit Clusters
SDC1 Hit Clusters

Event Reconstruction

Once a candidate single stub or stub pair is identified, additional algorithms are applied to determine:

Primary decay plane $\measuredangle$	Vertex to Vertex Dist.
Secondary decay plane $\measuredangle$	Stub to Vertex DOCA
Primary to Secondary decay plane $\measuredangle$	Transverse Momentum
Stub to Decay Plane $\measuredangle$	$M_{K_{\mu\mu e}}$
Stub to Stub Opening $\measuredangle$	$M_{K_{\mu\mu ee}}$
Tracking corrections	Tracking uncertainties

Invariant mass for the full event is then calculated in an N-body fashion based on the number of Tracks/Stubs available:

$$M^2 = \sum_{i=1}^{N} m_i^2 + 2\sum_{i=1}^{N}\sum_{j>i}^{N}\left(E_iE_j - |P_i||P_j|\sum_{k=1}^{D} a_{ik}a_{jk}\right) \tag{50}$$

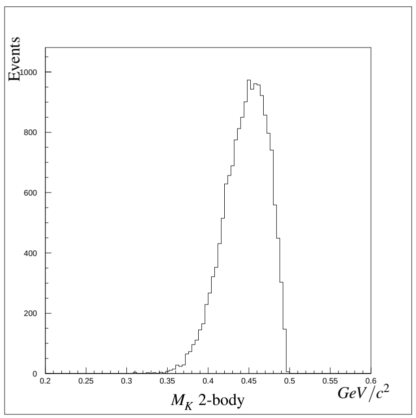

(a) 2-body invariant mass reconstruction

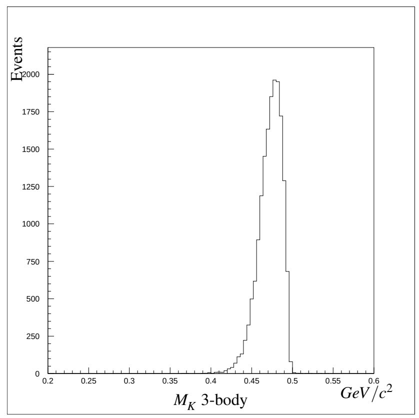

(b) 3-body invariant mass reconstruction

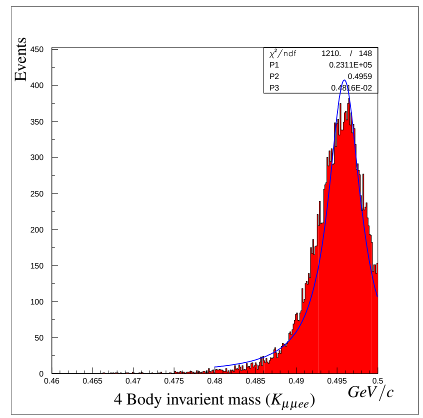

(c) 4-body invariant mass reconstruction

Collinearity and P_T

Most e^+e^- stubs are not momentum analyzed in the spectrometer magnets due to the soft momentum spectrum and resulting trajectory.

For these events we recover the e^+e^- momentum through the angular collinearity of the pair momentum vector with the target-vertex axis.

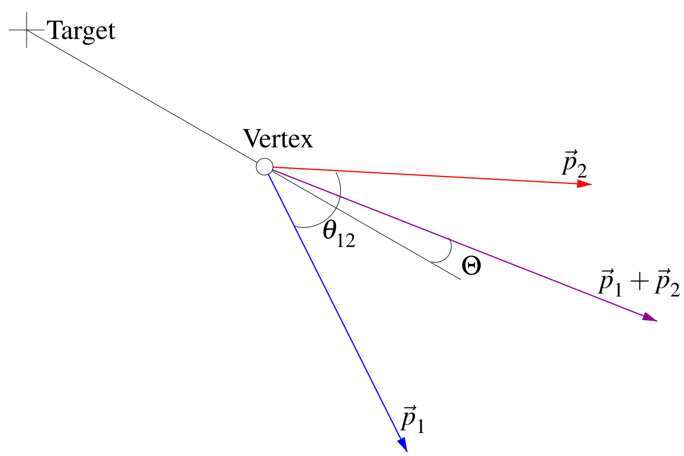

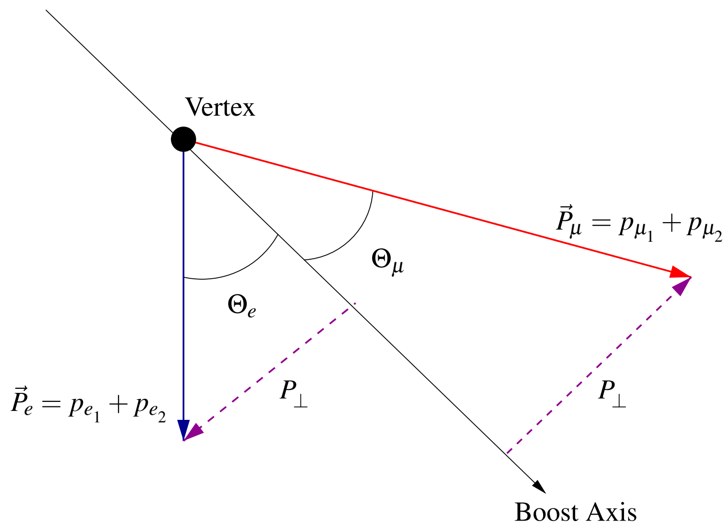

FIG. 46: Muon pair transverse momenta to electron pair transverse momenta sum relation through the collinearity angles Θ_μ and Θ_e

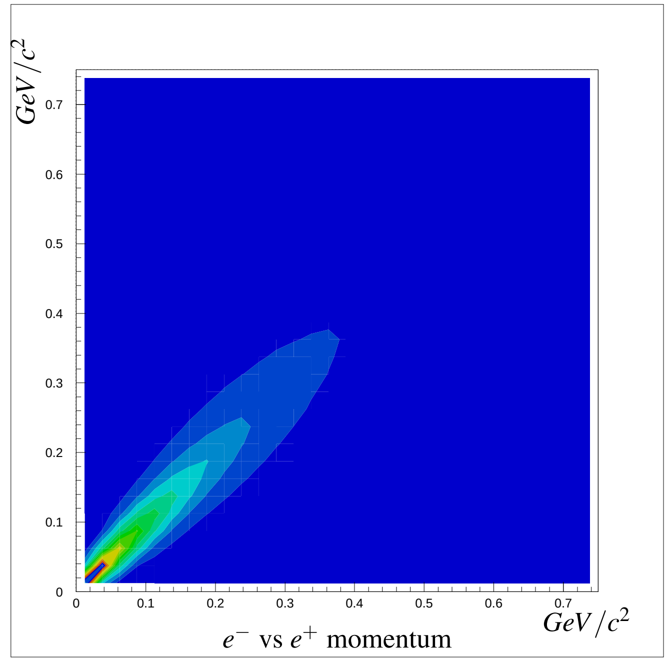

FIG. 47: e^- to e^+ low energy momentum asymmetries for $K_L^0 \to \mu^+\mu^-e^+e^-$

We recover an approximate electron pair momenta in fashion:

$$p_{e_{1,2}} \approx \frac{1}{2} P_e = \frac{|\vec{P}_\mu|}{2} \frac{\sin\Theta_\mu}{\sin\Theta_e} \tag{51}$$

- Using this momenta we compute vertex invariant mass and p_T again.
- These new $M_{K_{\mu\mu ee}}$ and p_T' form the basis for the primary signal box with tight constraints, similar to the $K_L^0 \to \mu^+\mu^-$ signal box.
- Uncorrelated events either fail the stub and vertex criteria or are forced to fall outside the signal region by the reconstruction algorithm

Part VII

Production Analysis

Data Sets

The production analysis involved building ntuples from the original $\mu\mu$ data strip.

Data ntuples were built forming both a $K_L^0 \to \mu^+\mu^-$ data set and a $K_L^0 \to \mu^+\mu^-e^+e^-$ data set with no event overlap between the two streams.

- $K_L^0 \to \mu^+\mu^-$ Ntuple consisted of 1,015,209 candidate events
- $K_L^0 \to \mu^+\mu^-e^+e^-$ Ntuple consisted of 159,018 candidate events

This is an overall reduction from the 1.8 terra bytes of data representing the initial E871 collected data.

This represents a single event sensitivity $\approx 5 \times 10^{-12}$.

$K_L^0 \to \mu^+\mu^-$ Cuts

The $\mu\mu$ Data set was subjected to the series of cuts in Table 5 to obtain the $K_L^0 \to \mu^+\mu^-$ signal peak for both the FT and QT fitters.

Vertex Parameter	Cut (FT)	Cut (QT)
V_x	± 2.7 mrad	± 2.7 mrad
V_y	± 10.0 mrad	± 10.0 mrad
V_z	$>$ 9.55 meters	$>$ 9.55 meters
V_z	$<$ 20.6 meters	$<$ 20.6 meters

Track Momentum	Cut (FT)	Cut (QT)
$P_{\mu^\pm}$	$>$ 1.05 GeV/c	$>$ 1.05 GeV/c
$P_{\mu^\pm}$	$<$ 6.50 GeV/c	$<$ 6.50 GeV/c

Track Momentum	Cut (FT)	Cut (QT)
Track χ^2	25	35

Event Vertex	Cut (FT)	Cut (QT)
Vertex χ^2	30	15

Mass Resolution	FT	QT
σ_{M_K}	1.26 MeV/c^2	1.43 MeV/c^2

Invariant Mass ($K_{\mu\mu}$)	Cut (FT)	Cut (QT)
$M_{K_{\mu\mu}}$	$>$ 493.5 MeV/c^2	$>$ 493.0 MeV/c^2
$M_{K_{\mu\mu}}$	$<$ 502.0 MeV/c^2	$<$ 502.5 MeV/c^2

Transverse Momentum	Cut (FT)	Cut (QT)
p_t	$<$ 0.010 GeV/c	$<$ 0.010 GeV/c

TABLE 5: $K_L^0 \to \mu^+\mu^-$ Analysis Cuts

$K_L^0 \to \mu^+\mu^-$ Signal Peak (FT)

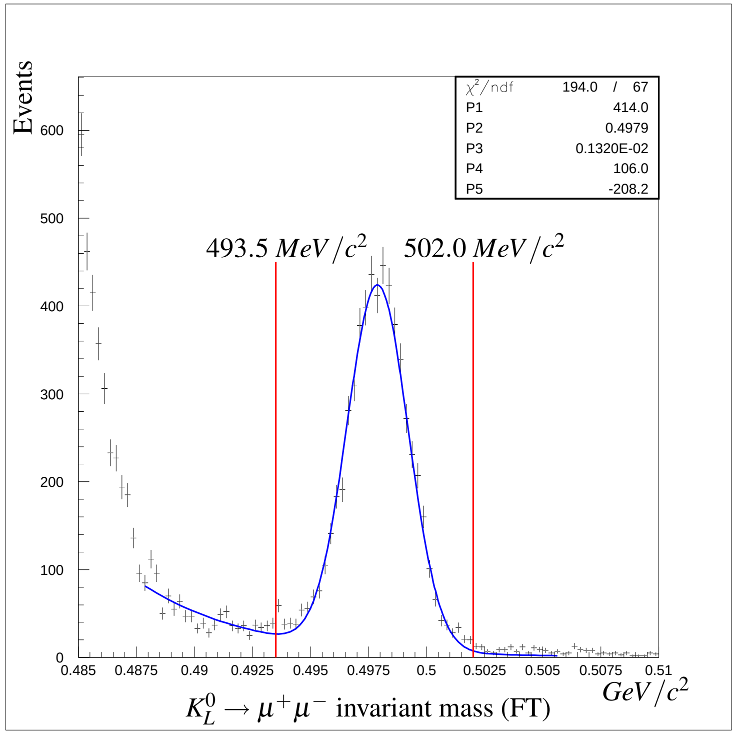

FIG. 48: $K_L^0 \to \mu^+\mu^-$ invariant peak showing 6069 events in the signal region consisting of 5657 ± 75 signal events on an exponential background of 412 ± 20 events.

$K_L^0 \to \mu^+\mu^-$ Signal Peak (QT)

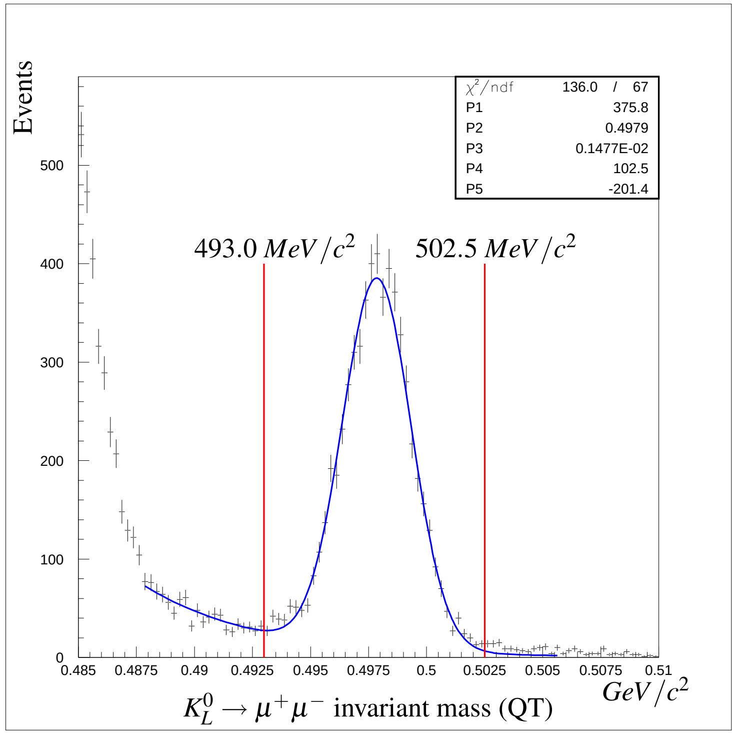

FIG. 49: $K_L^0 \to \mu^+\mu^-$ invariant peak showing 6133 events in the signal region consisting of 5714 ± 76 signal events on an exponential background of 419 ± 20 events.

$K_L^0 \to \mu^+\mu^-$ Events

It is determined that the number of $K_L^0 \to \mu^+\mu^-$ events in the data sample is 5685 ± 83

- Number of $K_L^0 \to \mu^+\mu^-$ events is less than E871 publication due a bad data tape from the Pass 3 output (0735 q2-q9,q16 roughly 7% of data)

Method	Signal	Background	Total
FT	5657 ± 75	412.43 ± 20.29	6069
QT	5714 ± 76	419.42 ± 20.47	6133
Average	5685 ± 83	415.5 ± 20.38	6101

TABLE 6: $K_L^0 \to \mu^+\mu^-$ signal and background events as observed in the E871 data set and reconstructed under FT and QT fitting.

$K_L^0 \to \mu^+\mu^- e^+e^-$ Cuts

Candidate events were subject to the cuts:

Cut Parameter	Value	Notes
V_x and V_x'	$\pm$2.7mrad	Beam Divergence
V_y and V_y'	$\pm$10.0mrad	Beam Divergence
V_z and V_z'	9.55 – 20.6meters	Decay Tank Volume
$P_{\mu^\pm}$	1.05 – 6.5GeV/c	High $\varepsilon_{\mu-ID}$ range
χ^2_{trk} (FT)	25	Track Fit
χ^2_{trk} (QT)	35	Track Match
χ^2_{vtx} (FT)	30	Vertex Fit
χ^2_{vtx} (QT)	15	Vertex Match
$M_{K_{\mu\mu}}$ (FT)	493.5 – 502.0MeV/c^2	$\mu\mu$ signal box veto
$M_{K_{\mu\mu}}$ (QT)	493.0 – 502.5MeV/c^2	$\mu\mu$ signal box veto
P_t	10MeV/c	$\mu\mu$ signal box veto
$\mu - ID$ $(Left/Right)$	$Good/Golden$	Parallel MRG only
Total Segments	1024	Reconstruction Limit
Total Stubs	4	Limit Event Noise
Stub to Vertex DOCA	9.27cm	$\varepsilon = 0.959$ $\sigma_\varepsilon = 0.0020$
Vertex to Vertex Dist.	10.59cm	$\varepsilon = 0.959$ $\sigma_\varepsilon = 0.0028$
Stub to Decay Plane $\measuredangle$	9.472°	$\varepsilon = 0.920$ $\sigma_\varepsilon = 0.0049$
Stub to Stub Opening $\measuredangle$	3.68°	$\varepsilon = 0.959$ $\sigma_\varepsilon = 0.0037$
Primary to Secondary Plane $\measuredangle$	15.8°	$\varepsilon = 0.993$ $\sigma_\varepsilon = 0.0015$
2-Body $M_{K_{\mu\mu}}$ (Low)	463.5MeV/c^2	Pion Mis-ID background
2-Body $M_{K_{\mu\mu}}$ (High)	502.5MeV/c^2	Unphysical $M_{K_{\mu\mu}}$
4-Body $M_{K_{\mu\mu ee}}$ (Low)	483.3MeV/c^2	Signal Box
4-Body $M_{K_{\mu\mu ee}}$ (High)	512.1MeV/c^2	Signal Box
4-Body P_t	12MeV/c	Signal Box

TABLE 7: Summary of Cuts for $K_L^0 \to \mu^+\mu^-$

$K_L^0 \to \mu^+\mu^-e^+e^-$ Signal Peak

The signal peak was found by applying the cuts in Table 7 to the 160,000 candidate events.

Additional particle identification was imposed to ensure a high event quality and reconstruction certainty:

- Strict Electron Veto in Čerenkov
- Strict Electron Veto in Lead Glass Calorimeter
- Parallel Muon ID in Muon Range Finder

Non-parallel muons in the MHO and TSCs were not considered due to trigger systematics ($> \pm 0.5$ counter widths and $> \pm$ 2 slats.)

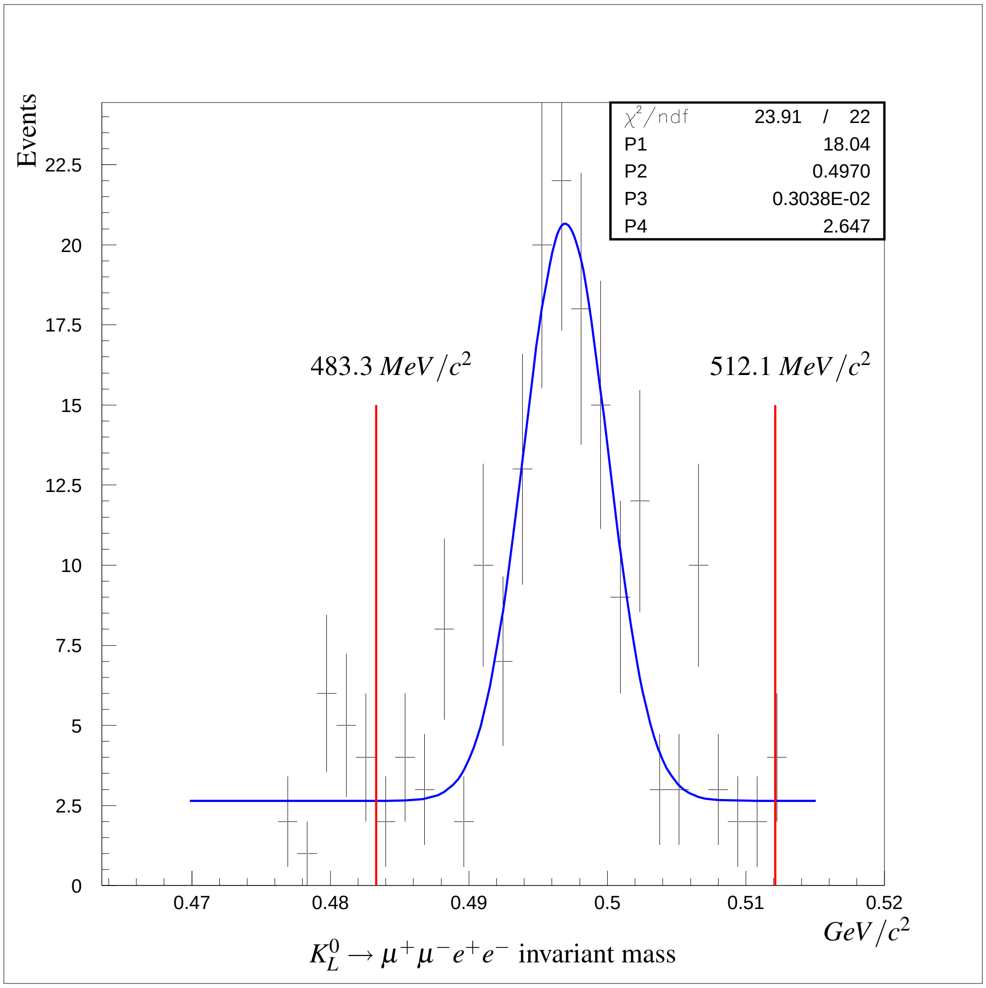

FIG. 50: $K_L^0 \to \mu^+\mu^-e^+e^-$ invariant peak showing 171 events in the signal region composed of 119 signal and 52 background

$K_L^0 \rightarrow \mu^+\mu^-e^+e^-$ Signal

The signal region was set a priori to extend from 483.3 MeV/c^2 to 512.1 MeV/c^2 based upon the width of the signal peak as reconstructed from Monte Carlo data with a set of "loose" cuts. ($\pm 3.5\sigma_{MC}$)

- Peak was fit to a Gaussian distribution on top of a flat background.
- Background was determined from linear fit to sidebands (< 488.3, > 512.1)
- Data was binning at 1.03 MeV/c^2.
- Centroid of the signal peak found at 497.0 MeV/c^2.
- Width of the signal peak found to be 3.04 MeV/c^2.
- Monte Carlo using *production* cuts predict 3.02 MeV/c^2 width!

Method	Signal	Background	Total
Loose	-	-	941
Parallel MRG	222 ± 20.7	57 ± 7.5	279
Strict Cuts/PID	119 ± 17.3	51.75 ± 7.2	171 ± 13

TABLE 8: $K_L^0 \rightarrow \mu^+\mu^- e^+ e^-$ signal and background events as observed in the E871 data set.

Signal Peak contained 119 satisfying the strongest signal criteria.

Background from K_{e3}, $K_{\mu 3}$ pileup contributed a flat background of 52 events.

Part VIII

Normalization

Branching Ratio

The branching ratio $B(K_L^0 \to \mu^+\mu^-e^+e^-)$ was calculated using the $K_L^0 \to \mu^+\mu^-$ data set for normalization.

$$\frac{B(K_L^0 \to \mu^+\mu^-e^+e^-)}{B(K_L^0 \to \mu^+\mu^-)} = \cdot \frac{N_{\mu\mu ee}}{N_{\mu\mu}} \cdot \frac{\mathscr{A}_{\mu\mu}}{\mathscr{A}_{\mu\mu ee}} \times \left(\frac{\varepsilon_{\mu\mu}^{L1}}{\varepsilon_{\mu\mu ee}^{L1}}\right) \times \left(\frac{\varepsilon_{\mu\mu}^{L3}}{\varepsilon_{\mu\mu ee}^{L3}}\right) \times \left(\frac{\varepsilon_{\mu\mu}^{\mu-ID}}{\varepsilon_{\mu\mu ee}^{\mu-ID}}\right) \times \left(\frac{\varepsilon_{\mu\mu}^{trk}}{\varepsilon_{\mu\mu ee}^{trk}}\right) \times \left(\frac{\varepsilon_{\mu\mu}^{vtx}}{\varepsilon_{\mu\mu ee}^{vtx}}\right) \times \left(\frac{1}{\varepsilon_{\mu\mu ee}^{stubs}}\right) \tag{52}$$

$\mathscr{A}_{\mu\mu ee}$ and$\mathscr{A}_{\mu\mu}$ are the Monte Carlo acceptances

ε^{cut} are the efficiencies for triggers and reconstruction

Acceptance Ratios

The ratio of acceptances is highly model dependent.

Theory	$\mathscr{A}_{\mu\mu}$	$\mathscr{A}_{\mu\mu ee}$	$\mathscr{A}_{\mu\mu}/\mathscr{A}'_{\mu\mu ee}$
χPT	1.900×10^{-2}	1.036×10^{-3}	18.329
QCD	1.900×10^{-2}	1.589×10^{-5}	1196.090
Uniform $(F=1)$	1.900×10^{-2}	1.224×10^{-6}	15522.876

TABLE 9: Acceptance Ratios for the form factor models considered in the $K_L^0 \to \mu^+\mu^-e^+e^-$ analysis.

Expected Events Per Model

The number of events expected under each model was calculated using the computed acceptances, the current world averages for the branching fractions, and the number of observed $\mu\mu$ events.

Theory	$\mathscr{A}_{\mu\mu}/\mathscr{A}'_{\mu\mu ee}$	Events
χPT	18.329	111.23
QCD	1196.090	1.70
Uniform $(F=1)$	15522.876	0.13

TABLE 10: Expected $K_L^0 \to \mu^+\mu^-e^+e^-$ Events

Branching Fraction

For 119 observed events the resulting branching fraction under the assumption of each model is calculated:

Theory	$B(K_{\mu\mu ee})$	σ statistical	σ systematic
χPT	2.78×10^{-9}	$\pm0.406\times10^{-9}$	$\pm0.091\times10^{-9}$
QCD	1.81×10^{-7}	$\pm0.265\times10^{-7}$	$\pm0.059\times10^{-7}$
Uniform ($F=1$)	2.36×10^{-6}	$\pm0.344\times10^{-6}$	$\pm0.077\times10^{-6}$

TABLE 11: $K_L^0\to\mu^+\mu^-e^+e^-$ normalized branching ratio for each of the form factor models considered in the $K_L^0\to\mu^+\mu^-e^+e^-$ analysis.

Results

- We have measured the branching fraction $\mathrm{B}(K_L^0 \to \mu^+\mu^-e^+e^-)$ based on an sample of 119 ± 17 events.
- The data is most consistent with enhancement of the high $\mu\mu$ invariant mass region, similar to that of a non-uniform form factor derived from chiral perturbation theory.

The branching fraction under this χPT hypothesis is:

$$B(K_L^0 \to \mu^+\mu^-e^+e^-) = 2.78 \pm 0.406 \pm 0.091 \times 10^{-9} \tag{53}$$

This is consistent with the world average to within 1 standard deviation.

Conclusions

- The measurement of $\mathrm{B}(K_L^0 \to \mu^+\mu^-e^+e^-)$ has provided a self consistent measure of the long distance dispersive amplitude, $\mathscr{A}_{LD}$.
- This should reduce systematic errors in the extraction of the Wolfenstein ρ.
- This measurement was also a sensitive probe into the structure of the $K_L^0 \to \gamma^*\gamma^*$ vertex and formfactors.
- The measurement provide strong evidence for the existence of a χPT formfactor.
- Additional investigation into the presence of chiral like formfactors in the kaon system should be conducted. In particular $K_L^0 \to e^+e^-e^+e^-$ and $K_L^0 \to \pi^+\pi^-e^+e^-$ should be examined.

Seminar Outline

References

[1] Ambrose *et al.*, Phys. Rev. Lett. **87**, 1398 (2000).

[2] D. Ambrose *et al.*, Phys. Rev. Lett. **81**, 4309 (1998).

[3] D. Ambrose *et al.*, Phys. Rev. Lett. **81**, 5734 (1998).

[4] J. Belz *et al.*, Nucl. Instrum. Methods **A**, 239 (1999).

[5] GU *et al.*, Phys. Rev. Lett. **76**, 4312 (1996).

[6] A. Alavi-Harati *et al.*, Phys. Rev. Lett. **87**, 111802 (2001).

[7] W. Molzon *et al.*, Technical report, Brookhaven National Laboratory AGS (unpublished).

[8] MECO collaboration and KOPIO collaboration, Technical report, Brookhaven National Laboratory AGS (unpublished).

[9] M. Kobayashi and T. Maskawa, Prog. Theor. Phys. **49**, 652 (1973).

[10] G. Rochester and C. Butler, Nature (London) **160**, 855 (1947).

[11] J. Christenson, J. Cronin, V. Fitch, and R. Turlay, Phys. Rev. Lett. **13**, 138 (1964).

[12] C. Caso *et al.*, European Physical Journal **C**, 010001 (1998).

[13] C. Geng and J. Ng, Phys. Rev. D **D41**, 2351 (1990).

[14] L. Bergström, E. Masso, P. Singer, and D. Wyler, Phys. Lett. **B134**, 373 (1984).

[15] P. Ko, Phys. Rev. D **45**, 174 (1992).

[16] J. O. Eeg, K. Kre*š*imir, and I. Picek, preprint (unpublished).

[17] G. Ambrosio, G. Isidori, and J. Portol*é*, Phys. Lett. **B**, 385 (1998).

[18] P. Skubic *et al.*, Phys. Rev. D **18**, 3115 (1978).

[19] T. Miyazaki and E. Takasugi, Phys. Rev. D **8**, 2051 (1973).

[20] P. Ko, Phys. Rev. D **44**, 139 (1991).

[21] L. Zhang and J. Goity, Phys. Rev. D **57**, 7031 (1998).